# Dynamics of pattern coarsening in a two-dimensional smectic system

Christopher Harrison,* Zhengdong Cheng, Srinivasan Sethuraman, David A. Huse, and Paul M. Chaikin
*Department of Physics, Princeton University, Princeton, New Jersey 08544*

Daniel A. Vega,† John M. Sebastian, and Richard A. Register
*Department of Chemical Engineering, Princeton University, Princeton, New Jersey 08544*

Douglas H. Adamson
*Princeton Materials Institute, Princeton University, Princeton, New Jersey 08544*
(Received 12 November 2001; published 29 July 2002)

We have followed the coarsening dynamics of a single layer of cylindrical block copolymer microdomains in a thin film. This system has the symmetry of a two-dimensional smectic. The orientational correlation length of the microdomains was measured by scanning electron microscopy and found to grow with the average spacing between $\pm\frac{1}{2}$ disclinations, following a power law $\xi_2(t)\sim t^{1/4}$. By tracking disclinations during annealing with time-lapse atomic force microscopy, we observe dominant mechanisms of disclination annihilation involving tripoles and quadrupoles (three and four disclinations, respectively). We describe how annihilation events involving multiple disclinations result in similarly reduced kinetic exponents as observed here. These results map onto a wide variety of physical systems that exhibit similarly striped patterns.

DOI: 10.1103/PhysRevE.66.011706 PACS number(s): 61.30.−v, 36.20.−r

## I. INTRODUCTION

### A. Motivation

Striped patterns are produced by a variety of mechanisms, including Rayleigh-Benard convection, ferrimagnetic repulsion in garnet films, and biological growth such as that displayed by a zebra's stripes [1]. The simplest realization of a nondriven striped system is the two-dimensional (2D) smectic liquid crystal, which consists of liquidlike order along one axis and a mass density wave along an orthogonal axis [Fig. 1(a)]. Though there are few suitable experimental realizations of this system, it has been a focus of theoretical work since being discussed by several seminal papers two decades ago [2–4]. In equilibrium and at a nonzero temperature, a 2D smectic is predicted to have short-range translational order with quasi-long-range orientational order. A Kosterlitz-Thouless transition is predicted to occur as disclinations unbind at elevated temperatures, destroying orientational order [5,6]. [Figure 1(b)]. However, little is known about the kinetics and mechanism by which order evolves in a 2D smectic or striped system after being quenched from the disordered state, the focus of this work. This is experimentally relevant as many systems are quenched from the disordered region of the phase diagram and the degree of order depends largely upon the controlling parameters of kinetics, e.g., time, temperature, and boundary conditions rather than thermodynamic quantities.

An experimental system possessing the symmetry of a 2D smectic must meet certain rigorous conditions for elucidating pattern coarsening dynamics. The optimal experimental system must be easily imaged, large enough to produce dislocations and disclinations (translational and orientational topological defects, discussed in Sec. II E), free from edge effects, and either be freely suspended or tailored such that the microstructures do not couple to any potential field from a substrate. Since translational order is precluded thermodynamically in a 2D smectic it is the development of orientational order which dominates the pattern coarsening kinetics [3]. As we shall show, the growth of orientational order is dominated by the annihilation of disclinations. Previous investigations have been limited to smaller systems (e.g., Rayleigh-Benard convection cells) with less than $10^2$ repeat spacings. These allowed for the study of dislocation interactions but not that of disclinations. Without investigating the interaction of disclinations, the full story of pattern coarsening could not be elucidated. In contrast, our use of a copolymer system has satisfied all of these constraints and allowed us to examine coarsening in a system with a lateral extent greater than $10^5$ repeat spacings. This system contains up to $10^8$ disclinations with a dislocation density approximately an order of magnitude higher. By tracking and analyzing the motion and annihilation events of both types of defects simultaneously we develop insight into the dominant mechanisms of coarsening. We measure and explain a $t^{1/4}$ power law for the growth of the correlation length via an unexpected coarsening mechanism involving annihilation events involving multiple disclinations.

### B. Block copolymer microdomains as a model 2D smectic

Block copolymers consist of two or more homogeneous but chemically distinct blocks that have been connected with a covalent bond. For components that are sufficiently dissimilar, microphase separation occurs in the melt where the volume fraction largely sets the microdomain morphology,

*Author to whom correspondence should be addressed. Permanent address: Polymers Division, Mailstop 8542, 100 Bureau Drive, National Institute of Standards and Technology, Gaithersburg, MD 20899.

†Permanent address: Department of Physics, Universidad Nacional del Sur., Av. Alem 1253, 8000-Bahia Blanca-Argentina.

 

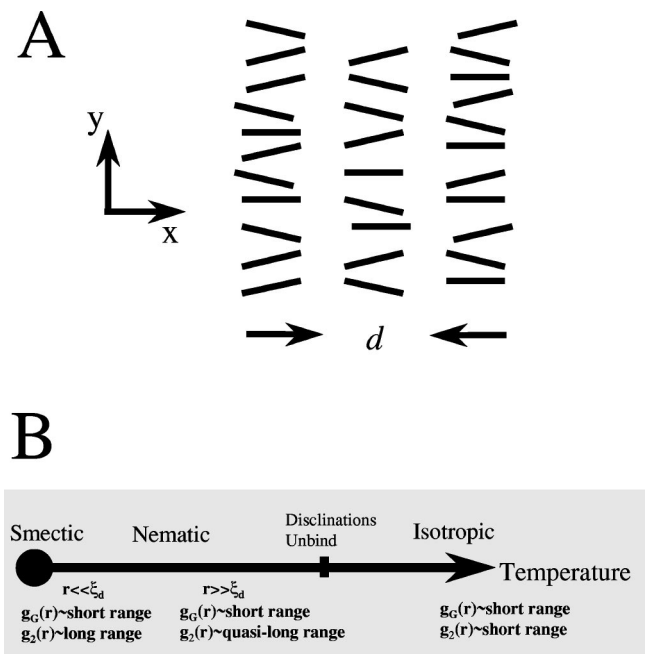


FIG. 1. (a) The smectic *A* phase where the nematogens (rodlike species) periodicially arrange themselves (repeat spacing $d$) along the $\hat{x}$ direction to form a mass density wave but with liquidlike order along the $\hat{y}$ direction. A 2D smectic consists of one layer of nematogens (shown) but for a 3D smectic the regions of high mass density extend into and out of the page. While nematogens have traditionally consisted of nanometer-sized hydrocarbons, copolymers with significantly longer chains produce structures with similar symmetries. (b) At zero temperature, 2D smectics exhibit long-range orientational and translational order. We indicate the respective correlation functions here as $g_2(r)$ and $g_{\mathrm{G}}(r)$. At nonzero temperatures and at length scales less than average spacing between dislocations (denoted $\xi_d$), thermal fluctuations lower the translational order to short range while maintaining long-range orientational order. At greater length scales (greater than $\xi_d$), dislocations lower the orientational order to quasi-long-range. A Kosterlitz-Thouless transition consisting of disclination unbinding occurs at a critical temperature, destroying orientational order. The critical temperature is close to the order-disorder temperature ($T_{ODT}$) for our copolymer system. Rather than focusing on equilibrium phenomena, we examine the kinetics of a copolymer system during pattern coarsening below its disordering temperature.

e.g., lamellas, gyroid, cylinders, or spheres. A good introduction to the history and physics of block copolymers can be found in the articles by Bates and co-workers [7,8]. A more recent review of the physics of thin copolymer films can be found in the work by Fasolka and Mayes [9]. Block copolymer morphologies adopt a polydomain configuration where the grains are on the order of microns. While these systems have been industrially useful in forming plastic elastomers for several decades, careful studies of the phase diagram have emerged only within the past decade. Investigations of microdomain morphology have been carried out via small angle x-ray scattering, neutron scattering, atomic force microscopy, and electron microscopy. Our work has focused on real-space studies of thin films of microdomains for their ultimate use as lithographic masks. To this end we developed techniques which quickly and reliably obtained images of microdomains in thin films (see Sec. II C) which are typically spun onto silicon wafers, a sample preparation method incompatible with traditional transmission electron microscopy imaging techniques. In the course of this work, we ascertained that a single layer of cylindrical microdomains has the same symmetries as a 2D smectic system, which enables us to study the classic 2D smectic in an unexpected realization with the desirable properties mentioned in the preceding section. In what follows, we will develop the analogy between polymeric structures and classic liquid crystal symmetry.

Though standard smectic liquid crystals consist of a mass density wave with a single molecular component, two component systems (such as the two blocks of our model copolymer system) create structures with consistent symmetries [10]. For example, copolymers that contain blocks of approximately equal volume produce lamellar microdomains in bulk [Fig. 2(a)]. This structure is the three-dimensional copolymer analog of the classical structure shown in Fig. 1, where the copolymer chain composition plays the role of mass density. The low and high mass density regions of Fig. 1(a) then, respectively, correspond to each of the two polymer blocks of Fig. 2(a). The amphiphilic nature of copolymers dictates that the repeat unit is two molecules, and is formally denoted smectic $A-2$.

The two-dimensional analog of this bulk copolymer structure would consist of a slice perpendicular to the shown planes with a thickness of approximately one radius of gyration so as to contain a single layer of polymers [schematized without showing the individual chains in Fig. 2(b)]. However, the well-known difference in the surface tensions of the two blocks would make such a structure difficult to create, as one block or another would preferentially wet the polymer-air or polymer-substrate surfaces [11]. Hence an alternative microdomain structure (cylindrical, produced by an asymmetrical copolymer where the minority block volume fraction is around 0.25) was employed, which consists of a single layer of cylindrical microdomains and is schematicized in Fig. 3(A). This schematic was previously ascertained by dynamic secondary ion mass spectrometry [12]. Here the polymer chains are not individually drawn but the light and dark regions of Fig. 2(a) correspond to the light and dark regions of Fig. 3(a). The cylinders consist of polymer block *A* (darker) in a matrix of *B* (lighter). Note that Fig. 1(b) is analogous to a cross sectional slice along the symmetry plane of Fig. 3(a). Cylindrical microdomains (and hence polymers) are confined in the thin film such that only lateral distortions and diffusion are possible. The cylindrical microdomains adopt an orientation parallel to the substrate due to wetting constraints and are characterized by a mass density wave consistent with the symmetries of the 2D smectic $A-2$ liquid crystal. Note also the polymer wetting layers on the top and bottom surfaces which separate the microdomain polymers from the surfaces [12,13]. Polymer chains that may be pinned at the interface by a chemical reaction therefore have a minimal effect on the motion of polymers in the microdomains. A representative scanning electron microscope image of the stripelike microdomains is shown in Fig. 3(b),

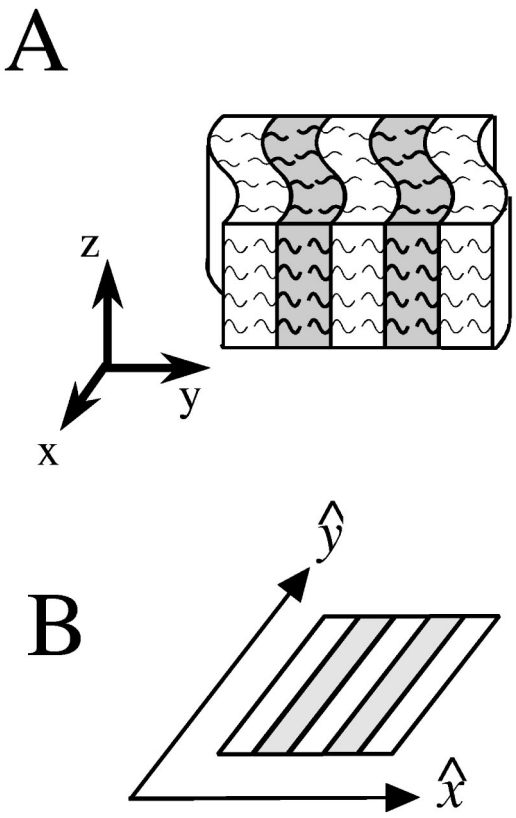


FIG. 2. (a) A symmetrical block copolymer melt, where each block occupies an equal volume fraction, produces a lamellar or smectic $A-2$ liquid crystal. Here we have schematicized one block with thick lines (dark background) and the other with thin lines (light background). The polymer chains adopt liquid order in the $\hat{x}$-$\hat{z}$ planes and a mass density wave perpendicular to the planes along the $\hat{y}$ axis. The amphiphilic nature of the polymer dictates that the repeat unit is two polymer chains. (b) The classic representation of a two-dimensional smectic where we denote regions of high and low mass density with dark and light regions. This two-dimensional smectic is consistent with a slice through panel (a) in the $\hat{x}$-$\hat{y}$ plane or $\hat{y}$-$\hat{z}$ plane, where the orientational undulations have been removed. We do not draw the chains here but denote the variation in chemical composition with the background color.

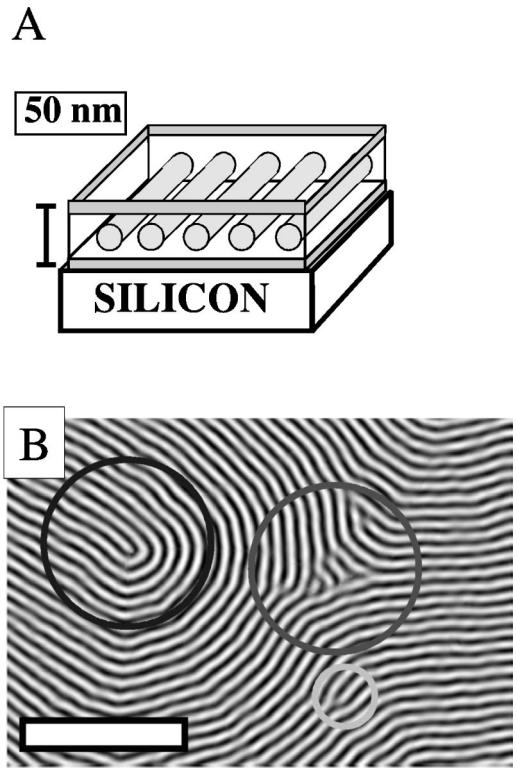


FIG. 3. (a) Schematic of one layer of polyisoprene (darker) cylinders in a polystyrene matrix on a silicon substrate. Note the layers of polyisoprene wetting the free and confined surfaces. The PI layer wetting the upper surface is uniformly removed by reactive ion etching to allow for optimal imaging of the cylinders underneath. Note that (b) is consistent with a slice though the midplane or symmetry plane of a single layer of cylinders, imparting the symmetry of a 2D smectic to these cylinders. (b) SEM image of cylinders lying parallel to the substrate, where contrast is provided by selective staining of the polyisoprene cylinders, which appear lighter in the image. A $+\frac{1}{2}$ disclination is centered in the left circle, a $-\frac{1}{2}$ disclination is centered in the right circle, and an elementary dislocation is enclosed in the smaller lower circle. Contrast has been enhanced by averaging the electron yield parallel to the cylinder axes. Bar=400 nm.

with several topological defects identified. The light and dark regions in the scarring electron microscope (SEM) micrograph of Fig. 3(b) correspond to a plan view of the cylinders and matrix in Fig. 3(a). The larger length scale of the repeat unit (tens of nanometers) of block copolymer systems over traditional nanometer-sized liquid crystals allows for surprisingly greater ease in high resolution imaging (either by atomic force or scanning electron microscopy), facilitating our experimental work.

Since an entire three-in silicon wafer can be coated with a single layer of 20-nm-sized microdomains, the sample spans an extent of $10^6$ repeat spacings. In practice $\frac{1}{2}$-in-sized pieces were used but these smaller samples still span an extent greater than $10^5$ repeat spacings. To our knowledge, block copolymer systems are the only nondissipative striped systems where edge effects can be fully negated (via the large system size) and thousands of disclinations can be observed, making them optimal for studying coarsening dynamics. However, the 20 nm length scale also has the drawback that nonoptical techniques are needed for imaging purposes, forcing one to use more time-consuming scanning techniques which are not truly *in situ*. However, the complementary techniques of atomic force microscopy and scanning electron microscopy provide sufficient information to measure both the kinetics and dynamics, albeit separately.

### C. Previous studies of kinetics with block copolymers

Though the fundamental morphologies of block copolymer microdomains have been well studied for decades, the factors that determine the range of orientational and translational order (grain size) have only recently been examined. Ordering kinetics have been examined in bulk samples, but a mechanistic understanding of coarsening dynamics has failed to emerge. Coarsening kinetics in polystyrene-polyisoprene

systems have been studied by Balsara and co-workers in 3D via depolarized light scattering [14,15], finding a slowing of grain growth with time, which was suggested to occur via the pinning of microdomains at grain boundaries. Using a similar technique, Amundson and Helfand studied the development of order in a polystyrene-poly(methyl methacyrlate) copolymer system under the influence of an electric field [16]. Calculations were carried out to examine the feasibility of various coarsening mechanisms under the influence of an electric field [10]. However, the lack of real-space observations on the dynamics limited these researchers' abilities to elucidate the dynamics. Additionally, these bulk (3D) studies introduced many complications concerning defect motion which are eliminated in 2D studies. Therefore we focus our research on real-space studies of the coarsening of copolymer microdomain patterns in thin films whose microdomain pattern is essentially two dimensional.

### D. Technological motivation

The most pressing application for understanding pattern formation in 2D smectics is block copolymer lithography—a process that uses self-assembled patterns (such as single layers of cylinders or spheres) as a template to fabricate devices at the nanometer length scale [17–19]. For example, when the 2D smectic template consisting of one layer of cylinders is used as a mask via block copolymer lithography, the correlation length (domain or grain size) of the ordered pattern dictates the length over which the cylinders can effectively be used as wires for connections. Alternatively, the addressability of an array of spheres for information storage depends upon developing translational order over large grains. Our motivation is therefore for both fundamental understanding of pattern coarsening and an application which we and other groups have used to pattern a variety of semiconductors [20], template metal ''necklaces'' for transport measurements [21], produce an unprecedented density of metal dots for information storage [22], and most recently, fabricate InGaAs/GaAs quantum dots for laser emission [23].

### E. Controlled means of ordering

While we focus here on pattern development and the growth of grains, other efforts have developed means of controlling microdomain orientation. Jaeger and co-workers [24] controlled the microdomain orientation in thin films in small regions (square microns) with isolated electrodes, and this has been more recently extended to larger areas with an interdigitated set of electrodes [25]. Thurn-Albrecht and coworkers have used electric fields from parallel platelike electrodes to macroscopically orient a thin film of cylindrical microdomains over macroscopic areas (square centimeter) to align perpendicular to the substrate [26,27]. Segalman, Yokoyama, and Kramer have recently examined the influence of an edge on the alignment of spherical micrdomains [28]. Additionally, macroscopic orientation of the copolymer microdomains in thin films is being investigated by directional crystallization and by applying pressure [29,30]. While these efforts are designed to control the local or macroscopic control of the microdomain orientation for the purposes of technological applications, this task will be aided by a pattern which is well ordered, the focus of this paper.

### F. Overview of paper

We present an overview of this paper's organizational layout here. In Sec. II we describe the polymer synthesis, thin film preparation, electron and atomic force microscopy imaging techniques, and methodology for correlation function measurements. In Sec. III, we examine the coarsening process by measuring the time dependence of the orientational correlation length, disclination density, and dislocation density. We show that the correlation length follows the average distance between disclinations, suggesting that disclination annihilation drives the coarsening process. Disclinations and dislocations are tracked in Sec. IV and multidisclination (greater than 2) annihilations are shown to drive the growth of the correlation length. Section V discusses a model that incorporates the observed coarsening process and results in a similar kinetic exponent as observed. We also compare our results with those from previous simulations and discuss further work along these lines, which warrants investigation. In Sec. VI, we attempt to extrapolate the equlibrium properties of the copolymer system by first showing the existence of long-range orientational order and short-range translational order. We use the strain fields of disclinations and dislocations to measure the ratios of elastic constants $K_3/K_1$ (bend/splay) and $K_1/\bar{B}$ (bend/layer compression). Finally, in Sec. VII we draw attention to the similarity of the microdomain pattern to that of fingerprints (dermatoglyphs) and discuss the relationship between pattern formation in the two systems.

## II. EXPERIMENT

### A. Polymer synthesis

Asymmetric polystyrene-polyisoprene (PS-PI) copolymers were synthesized via living anionic polymerization with a mass of 30 kg/mole for the PS block and 11 kg/mol for the PI block to form PI cylinders in a PS matrix [denoted SI 30-11, chemical structure shown in Fig. 4(a)] [31]. This copolymer was synthesized in a cyclohexane/benzene (90/10 v/v) mixture to yield a 90% 1,4 content in the polyisoprene block. The microdomains formed by this polymer were studied by scanning electron microscopy. Gel permeation chromatography (GPC) revealed a polydispersity of 1.04 and the absence of polymers, which inadvertently terminated before the addition of the second block. The upper glass transition temperature ($T_g$) was measured to be 367 K by differential scanning calorimetry (DSC).

For atomic force microscopy, another PS-PI diblock was synthesized and the polyisoprene block was saturated with hydrogen to form poly(ethylene-alt-propylene) [Fig. 4(b)] [32]. This hydrogenated copolymer, denoted PS-PEP 5-13, is less prone to degradation during annealing, as all double bonds were saturated. Small angle x-ray scattering confirmed that PS-PEP 5-13 consists of PS cylinders in a PEP matrix, the morphological inverse of SI 30-11. At room temperature, the PEP block is above its $T_g$ and is rubbery while the PS

A

polystyrene-polyisoprene

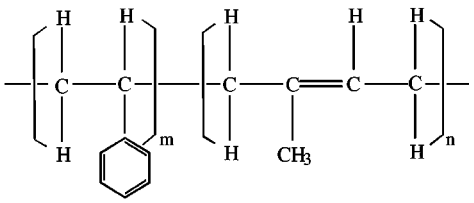


B

polystyrene-poly(ethylene-*alt*-propylene)

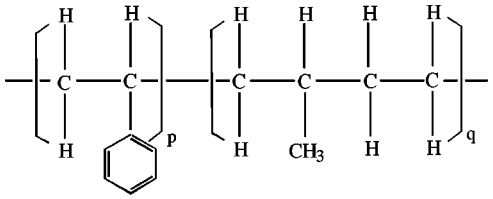


FIG. 4. Chemical composition of diblock copolymers and principal means of pattern investigation. (a) Polystyrene-polyisoprene (PS-PI 30-11) was investigated by scanning electron microscopy. The number of PS and PI monomers are indicated by *m* and *n* and are on average 286 and 162, respectively. (b) Polystyrene-poly(ethylene-alt-propylene) (PS-PEP 5-13) was investigated by atomic force microscopy. The number of PS and PEP monomers are indicated by *p* and *q* and are on average 48 and 186, respectively.

block is below its $T_g$ and is glassy. The higher of the two $T_g$'s is referred to as the upper $T_g$ and was measured by DSC to be 330 K. This difference in moduli of the two blocks gives rise to the contrast observed by atomic force microscopy. Since this is more novel than the synthesis employed in the previous diblock we include more detail here. The hydrogenation was conducted in cyclohexane at a polymer concentration of about 10 g/l in a 2-l Parr batch reactor. To selectively hydrogenate the polyisoprene block, a homogeneous Ni-Al co-catalyst was prepared by combining 30 ml of 0.1*M* nickel 2-ethylhexanoate in cyclohexane with 10 ml of 1.0*M* triethylaluminum in hexanes under a dry nitrogen atmosphere. The cocatalyst was injected into the reactor, and hydrogenation was carried out at 350–360 K and 400–500 psi hydrogen for 5 days. The catalyst was removed by vigorous stirring with a 10% solution of aqueous citric acid until the dark catalyst color disappeared. The polymer was then precipitated into acetone/methanol. Using 1 H nuclear magnetic resonance spectroscopy, the level of polyisoprene saturation was determined to be greater than 99% with no detectable saturation of the polystyrene block. GPC analysis revealed a polydispersity of 1.042. In certain cases, atomic force microscope images of the resulting copolymer revealed an unacceptably high level of remaining alumina particles. These were removed by repeating the citric acid wash.

While a strict comparison of the kinetics of these two copolymers would be inappropriate due to their different molecular weights, their segregation strengths are similar, suggesting that similar coarsening mechanisms would be at work in a thin film of either copolymer. To calculate the segregation strengths, we start with the interaction energy densities. The measured interaction energy densities for the PS-PI and PS-PEP copolymers, as obtained by Lai *et al.* are listed below [33]:

$$X_{PS\text{-}PI} = -0.30 + 1013/T, \tag{2.1}$$

$$X_{PS\text{-}PEP} = 0.57 + 1655/T. \tag{2.2}$$

We calculate the segregation strength $\chi N$ of the copolymer blocks via the usual equation below, where $R$ is the gas constant and $\rho$ is the average density of the copolymers,

$$\chi N = X(M_w/\rho RT). \tag{2.3}$$

Using the average densities of these copolymers as presented by Fetters and co-workers, $\chi N = 28$ at 413 K for both copolymers, the middle of the three temperatures examined here [34].

Though the molecular weights of the two copolymers studied here differ by a factor of 2, their repeat spacings ($d$, distance from adjacent cylinder centers) differ by no more than 25%. The repeat spacing for SI 30-11 is 25 nm (as measured by SEM) and 20 nm for PS-PEP 5-13 [as measured by atomic force microscopy (AFM)]. Both of these systems are strongly segregated ($\chi N \gg 10$, where $N$ is the number of monomers per chain), for which the repeat spacing depends upon molecular weight as

$$d \sim M_w^{2/3} \chi^{1/6} b, \tag{2.4}$$

where $b$ is the statistical segment length [35]. While the large difference in molecular weights favors a disparate repeat spacing, it is mitigated by both the interaction parameter $\chi$ and the statistical segment length $b$ in the above equation to produce copolymers with similar repeat spacings [34].

### B. Wafer treatment and spin coating

Silicon wafers (Silicon Quest International) were cleaned by vigorous washing in boiling acetone, trichloroethylene, and isopropyl alcohol. The native oxide was dissolved by a brief dip in buffered oxide etch and then reoxidized with pure nitric acid. The details of this procedure can be found in an earlier publication [36]. Copolymers were applied to carbon-coated (Denton Vacuum carbon coater, model DV-502) or bare silicon substrates via spin coating from a dilute solution (typically 1%) in toluene, a good solvent for both blocks. The thickness of one layer of cylindrical microdomains for SI 30-11 was 50 nm. The thickness of one layer of cylindrical microdomains for PS-PEP 5-13 was 30 nm. After annealing, terracing at discrete thicknesses was observed in spin-coated samples of noncommensurate thicknesses [37]. Sample sizes were typically on the order of a 1 cm.

### C. Microscopy techniques employed

Both SEM and AFM were employed as complementary techniques to characterize pattern coarsening. The SEM has the ability to obtain high resolution images of large areas of the sample, making it suitable for accurate correlation length measurements. SEM images also suffered from less distortion (such as skew) than AFM images. However, the osmium tetroxide staining process used to provide electron contrast arrests all polymer dynamics, making it unsuitable for studying the dynamics of individual defects. Additionally, the polymer film etching necessary for optimal imaging damages the polymer chains (see Sec. II C 1). Disclination and dislocation motion, therefore, were studied by time-lapse AFM using a method that does not alter or damage the sample. While the AFM could, in principle, measure grain sizes by stitching together many high resolution images of small areas, in practice this tends to be impossible due to distortions in the image due to hysteresis of the piezos used for positioning the sample. While the mechanisms of image generation differ dramatically from SEM to AFM, the cylinders appear lighter for both cases and hence all images presented here. We organize the remainder of the sample preparation techniques along the microscopy technique employed.

#### *1. Scanning electron microscopy*

For scanning electron microscopy, order was induced through vacuum annealing (better than $10^{-5}$ torr) above the glass transition temperature (measured by differential scanning calorimetry as 367 K). The vacuum probe consisted of an aluminum pipe (chosen for its good thermal conductivity) evacuated with an oil-based diffusion pump backed with a roughing pump. Aluminum shelves were attached to the inside of the pipe for placement of copolymer-coated silicon wafer samples. Good thermal contact between the silicon wafers and the stage was assured by liberal use of thermal grease. The temperature was monitored by a thermistor and the pressure was monitored by an ion discharge tube [38]. The vacuum pipe had a skirt built around it to seal the front of a vacuum oven (Fisher Scientific Model 280), in effect functioning as the oven door. Vacuum annealing produced a pattern which is schematically shown in Fig. 3(a). After annealing, microdomains were preferentially stained with vapors of $OsO_4$ (Polyscience, Inc.) for at least 2 h to provide contrast for electron microscopy. The microdomain pattern was examined with an imaging technique which uniformly etches away the surface of the structure schematized in Fig. 3 for imaging with a SEM. The details of the etching and imaging technique employed can be found elsewhere, but we briefly describe the procedure here [12,39,40]. Optimal imaging contrast was found by etching away 12 nm of the polymer film with low power, low pressure, $CF_4$-based reactive ion etching [39] (Applied Materials, Inc.) to expose the microdomains to the surface. Images of the exposed microdomains were then obtained with a low voltage, high resolution Zeiss 982 SEM. Optimal imaging was typically found with an operating voltage of 1 kV, a 3 mm working distance, a spotsize of 3, and by mixing both secondary and backscattered electrons. The SEM allowed us to image large areas of the polymer film at high resolution for accurate measurements of the average grain size. As $OsO_4$ staining arrests the coarsening process, multiple specimens were annealed in parallel for varying times prior to staining to follow the coarsening kinetics. Figure 3(b) shows a representative image where the stained PI cylinders appear lighter due to a higher electron yield and can be seen lying parallel to the substrate. The microdomain repeat spacing $d$ is 25 nm, as measured from the wave number of dominant intensity in Fourier space. The longest annealing time attainable during our experiments is limited by the onset of polymer degradation, which occurred sooner at higher annealing temperatures. Polymer degradation was monitored by gel permeation chromatography analysis of polymers annealed in parallel. Polymer degradation was immediately evident with SEM as a diminished contrast between the stained microdomains and matrix. Further annealing and hence degradation resulted in disordered microdomains, and in some cases, evolution of cylinders to disordered spheres. We report here data only from polymers which exhibited no degradation.

#### *2. Atomic force microscopy*

For atomic force microscopy, spin-coated samples were imaged at ambient temperature, annealed above the upper $T_g$ in air on a temperature-controlled heater stage mounted on the AFM [41]. and then reimaged after cooling. Phase contrast between the microdomains and the matrix disappeared for temperatures above the upper $T_g$, suggesting that phase contrast originates from the difference in moduli of the two blocks. By repeating this cycle dozens of times and reimaging the same area we observed the annihilation processes of disclinations. While previous AFM investigations of block copolymers have investigated the microscopics of microdomain joining and scission [42], we focused our attention on events concerning defect annihilation where the pattern is sufficiently well ordered that identification of topological defects is straightforward. To this end samples were annealed at temperatures up to 383 K for many hours to produce well-ordered patterns. While annealing unsaturated polydienes under these conditions in air typically causes degradation, here the saturated PEP showed no evidence of degradation.

We chose to study the relatively low molecular weight PS-PEP 5-13 (compared to SI 30-11) via AFM because its smaller chain length minimizes the distance between the surface and the microdomains thereby facilitating satisfactory imaging. While microdomains submerged beneath the surface can be easily imaged for this low molecular weight PS-PEP copolymer, the larger length scale of higher molecular weight copolymers of similar chemical composition was shown to submerge the microdomains sufficiently below the top surface such that images of the microdomains were impossible to obtain. This was demonstrated by comparing two PS sphere forming copolymers, the lower molecular weight PS-PEP 3-22 (synthesized in a manner consistent with PS-PEP 5-13), and the much higher molecular weight PS-PI 10-69, a commercially available diblock copolymer (synthesized by Gary Marchand for Dexco Polymers). AFM scans of the free surface of PS-PI 10-69 copolymer films (prepared as described in Sec. II,B) yielded little or no contrast of the

microdomains underneath. SEM scans of $OsO_4$ stained samples yielded similar results. While we were able to etch away the surface wetting layer to subsequently image the submerged microdomains (as with the RIE/SEM technique) via AFM or SEM, this damaged the copolymer chains and altered the sample chemistry. However, the lower molecular weight PS-PEP 3-22 copolymer produced excellent phase contrast by AFM without reactive ion etching. The line to line repeat spacing of hexagonally packed PS spheres in a PI or PEP matrix, as measured by the dominant wave number in Fourier space, was 22 nm for PS-PEP 3-22 and 33 nm for PS-PEP 10-69. Evidently this 50% increase in repeat spacing dramatically decreases the ability to sense microdomains as it shifted the thickness for one layer of microdomains from 30 nm to 60 nm for 3-22 and 10-69, respectively By selecting copolymers with lower molecular weights (such as PS-PEP 5-13), the distance from the microdomains to the free surface is reduced and the tip can obtain satisfactory images without etching.

Tapping mode AFM (Digital Instruments model IIIA) was employed with tapping mode OTESPA (Digital Instruments) silicon tips. Each tip was initially tuned so as to find a suitable resonance frequency, usually around 250 kHz. The RMS target amplitude during tuning was set with a corresponding magnitude of 2 v. The RMS amplitude of the piezo-driven tip typically decreased by about 25% upon engaging [43]. For the purposes of optimal imaging, either the drive amplitude was increased or the set point was decreased until satisfactory images were obtained. The magnitudes of these changes varied from tip to tip. Optimal contrast was found with phase mode imaging though microdomain contrast was observed in height images when the AFM was operated with a high drive amplitude. Care was taken to operate the AFM with the least amount of tapping force as higher driving amplitudes scored the polymer film. On average one out of three tips as purchased produced satisfactory images. Though the tip holder was removed during annealing to prevent deposition of vapors on the tip, we found upon replacing the tip holder that registry could be maintained to better than 2 $\mu$m. Further registry during each annealing cycle was obtained with the low density of fiducial marks consisting of alumina particles introduced by the hydrogenation process. In certain cases, aqueous solutions of silica particles were spin coated on the PS-PEP films to act as additional fiducial marks.

Though satisfactory AFM images of block copolymer microdomains were obtained where the matrix was rubbery, we were unable to obtain images from copolymers where the matrix was glassy [such as with SI 30-11 shown in Fig. 3(a)]. We suggest that the tip was unable to penetrate the glassy polystyrene matrix in this case to sense the rubbery microdomains underneath.

### D. Data analysis: Correlation length measurements

Data analysis of SEM or AFM images was performed with algorithms written in VISUAL C++ (Microsoft) on a PC-clone computer [36,44]. We describe our algorithms briefly here. Zeiss SEM images (typically $1024\times768$ pixels) were directly saved as 8-bit gray scale TIFF file formats. AFM images ($512\times512$ pixels) were flattened (third order polynomial fit), contrast enhanced, and then exported as similar TIFF files. All images were then Fourier filtered to remove high frequency noise and low frequency intensity variation. Next, the microdomain cylinder orientation was obtained by measuring the local intensity gradient (averaged over an area of $d^2$). To enhance contrast in some cases, the intensity fields of microdomain images were locally averaged along the direction of the microdomains, which provided a surprisingly good improvement to the image quality. Correlation functions were measured only from images without such local directional smoothing. We produce an orientational field $\theta(\vec{r})$ for each image while taking account of the twofold degeneracy of this cylinder in orientation with respect to its gradients [44]. With this field we generate a continuous order parameter field $\psi(\vec{r})$, defined as below,

$$\psi(\vec{r}) = \exp[2i\,\theta(\vec{r})], \tag{2.5}$$

where $\vec{r}$ is position and $\theta$ is the microdomain orientation (similar to a director) [36].

The orientational correlation function $g_2(r)$ was then calculated from the order parameter field in the usual way, where the angular brackets below imply averaging correlation pairs at a given distance over all angles. We note that the correlation function was directly calculated from correlation pairs, rather than via by converting to Fourier space via the usual Wiener-Khintchine shortcut to avoid introducing any artifacts in the correlation function, especially at large separation distances [45],

$$g_2(|\vec{r}|) = \langle \psi(\vec{0})\,\psi(\vec{r})\rangle. \tag{2.6}$$

The orientational correlation length $\xi_2$ was measured by fitting $g_2(|\vec{r}|)$ with $e^{-|\vec{r}|/\xi_2}$. Error bars were estimated by the variation in $\xi_2$ from the many images taken of each sample.

We also measured the orientational correlation lengths both parallel ($\xi_\parallel$) and perpendicular ($\xi_\perp$) to the microdomain axis orientation. This was done by locally measuring the microdomain orientation at each position and then measuring the decay of the correlation intensity $g_2(r)$ parallel to the microdomain and perpendicular to the microdomain, respectively. Checks were performed on artificially created images (such as stripes with a uniform orientation) to verify that these correlation functions were rigorously defined.

The translational order parameter was determined by choosing a region free from disclinations and Fourier transforming to measure the dominant wave number $\vec{G}$. It was found to be more convenient to macroscopically orient the cylinders to be parallel to one axis of the image so that only one component of $\vec{G}$ was nonzero. The image was then thresholded and skeletonized (Image Processing Toolkit, by Reindeer Games, running in Adobe PHOTOSHOP5.5) to locate the center of the cylinders. We conventionally define the translational order parameter as

$$\psi_{\vec{G}}(\vec{r}) = \exp[i\vec{G}\cdot\vec{r})]. \tag{2.7}$$

The translational correlation function $g_G(|\vec{r}|)$ was determined in the usual way. Again, the angular brackets implicitly imply averaging over correlation pairs with no preference to direction (azimuthally averaged),

$$g_G(|\vec{r}|)=\langle \psi_{\vec{G}}(0)\psi_{\vec{G}}(\vec{r})\rangle. \tag{2.8}$$

The translational correlation length $\xi_G$ was measured from the characteristic decay length of $g_G(|\vec{r}|)$ when fit to an exponential function.

The correlation functions were used to determine the range of translational and orientational order in the images. For accurate measurements of the range of short-range orientational order, mutiple images (typically four) of each sample were obtained from random sample locations well away from the edge. The size of the image and the resolution level was chosen such that the repeat spacing $d$ was at least six pixels and the width and height were at least ten correlation lengths.

#### E. Data analysis: Locating topological defects

Both orientational and translational defects were examined. To locate orientational defects, such as $\pm\frac{1}{2}$ disclinations, closed path integrals of the variation of the microdomain angle $\theta(r)$ were performed throughout the microdomain orientational field. If the integral over a counterclockwise closed path about a potential disclination core equalled $\pm\pi$, then it was identified as a disclination of the respective sign. This condition is formally written as (where $s$ is path length)

$$\oint \frac{\partial\theta}{\partial s}\partial s=\pm\pi. \tag{2.9}$$

For example, $+\frac{1}{2}$ disclinations were identified with paths consisting of $\pi$ rotations, $-\frac{1}{2}$ disclinations were identified with paths consisting of $-\pi$ rotations. The density of disclinations of either sign is denoted by $\rho_{\pm}$. Further details as to the actual implementation of this algorithm can be found in the thesis by one of us [44].

Elementary dislocations were identified by decomposition into two closely spaced $\frac{1}{2}$ disclinations of opposite sign [46]. The dislocation density is denoted $\rho_{\epsilon}$. Dislocations of all orientations were counted, and their proximity to disclinations was identified by calculating a dislocation-disclinaton correlation function $h(r)$,

$$h(|\vec{r}|)=\langle \rho_{\pm 1/2}(0)\rho_{\epsilon}(\vec{r})\rangle/\langle \rho_{\pm 1/2}(0)\rangle. \tag{2.10}$$

$h(|\vec{r}|)$ measures the dislocation density as a function of distance from a disclination of either sign. When counting dislocations, a proximity-based cutoff was imposed such that disclinations would not be identified as dislocations.

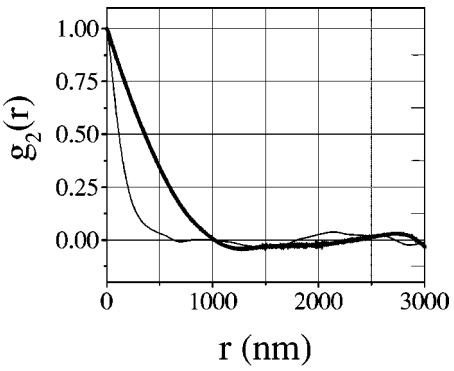


FIG. 5. Orientational correlation functions $g_2(r)$ for samples annealed for 1 h (thin line) and 111 h (thick line). The correlation functions are fit with an exponential decay $\exp(-r/\xi_2)$ and reveal correlation lengths of 145 and 478 nm for short and long times.

## III. COARSENING KINETICS

### A. Introduction

In order to characterize the coarsening kinetics, an entire 3-in. silicon wafer was spin coated with SI 30-11 from a dilute polymer solution (less than 1% by weight) at a thickness (50 nm) equal to one layer of microdomains. This was broken into many centimeter-sized samples, which were annealed in parallel. The as-cast microdomain pattern was disordered as confirmed by SEM and AFM. The rapid concentration of the polymer via evaporation during spin coating is analogous to a quench of the polymeric system from a disordered high temperature state to an ordered (albeit glassy) low temperature state. Samples were annealed for various lengths of time (1–300 h), stained, and examined by SEM to quantitatively characterize the degree of microdomain order. Many images were collected per sample at random locations to estimate the variance in the measured quantities. We report here the results on carbon-coated substrates, but films on bare substrates yielded consistent results but with a lower degree of order for the same annealing time, most likely due to a lower diffusion constant [44].

### B. Azimuthally Averaged Correlation Lengths

The azimuthally averaged orientational correlation length ($\xi_2$) of the cylindrical microdomain pattern was measured as a function of annealing time by fitting the orientational correlation function $g_2(r)$ with an exponential decay. Two sample correlation functions are shown in Fig. 5, where the thin line corresponds to a sample annealed for 1 h and the thick line to one annealed 111 h at 443 K. Correlation lengths of 145 and 478 nm were measured here and the increase in $\xi_2$ with time reflects the coarsening of the microdomain pattern during annealing.

Using this analysis technique, three annealing temperatures (443 K, 413 K, and 398 K) were examined and the time dependence of the correlation lengths are plotted in Fig. 6(a) as closed circles, open circles, and squares, respectively. For the upper two annealing temperatures, a power law can be seen where the best fits are shown with solid lines. The data is well fit by a power law $\xi_2(t)\sim t^{0.25\pm 0.02}$ at 443 K and a

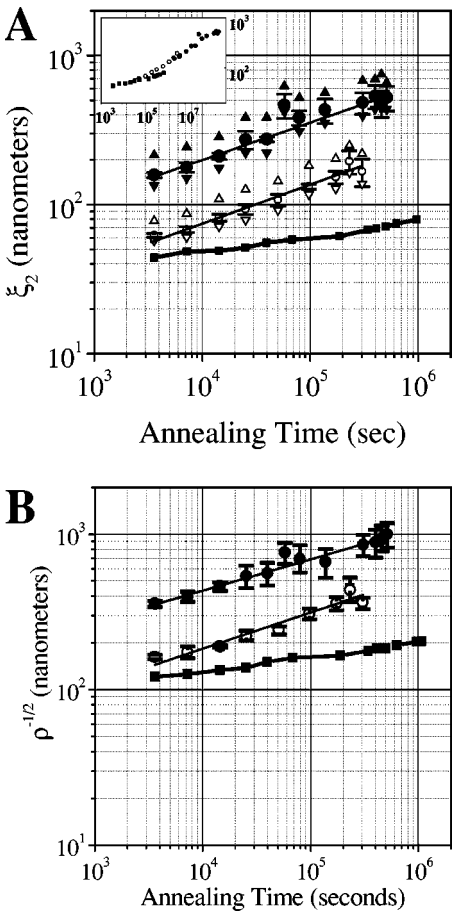


FIG. 6. (a) Orientational correlation length for SI 30-11 as a function of time. The lowest data set, consisting of filled squares, corresponds to 398 K. For the remainder of the data, the open symbols correspond to 413 K and the closed symbols correspond to 443 K. The solid lines are produced by fitting a power law to the data. The measured kinetic exponent for the 443-K data is $0.25 \pm 0.03$ and for the 413-K data is $0.25 \pm 0.03$. The 398-K data is closest to the glass transition temperature, which may explain its deviation from power law behavior. Data from this set was sufficiently disordered that topological defects were difficult to identify. Inset: Plot of $\xi_2(t)$ where the time axis for 413 K and 443 K have been multiplied by the WLF shift factors of 18 and 797 (see text). Symbols indicate same temperatures as in larger graph. Note that the correlation length for the two upper temperatures nicely falls on a master curve but the lower temperature does not. (b) The average spacing between disclinations as a function of annealing time for the data sets shown in panel (a). The closed circles correspond to 443 K, the open circles to 413 K, and the squares to 398 K. The interdefect spacing was measured from $\rho_{\pm}^{-1/2}$, where $\rho_{\pm}$ is the disclination density of the respective sign. Due to their similar values, almost all data points of $\rho_{+}^{-1/2}$ lie directly on $\rho_{-}^{-1/2}$ (not shown). Note that the correlation length increases with the same power law as that for the interdisclination spacing, implying that disclination annihilation dominates the coarsening process. Also note that the magnitudes of $\rho_{\pm}^{-1/2}$ are similar to $\xi_2$.

power law $\xi_2(t) \sim t^{0.25 \pm 0.02}$ at 413 K, suggesting a kinetic exponent of 1/4. Longer annealing times were prohibited by the onset of polymer degradation. For the lower temperature (398 K), the correlation length deviates from a power law dependence with a significantly lowered coarsening rate. The pattern is sufficiently disordered over the entire range of the 398 K anneal that the average spacing of topological defects is on the order of one repeat spacing $d=25$ nm and the interaction forces derived from linear elastic strain theory break down. Consequently, if the 1/4 exponent observed from the upper two annealing temperatures is produced by interactions of topological defects, we should expect a different coarsening exponent here, perhaps dominated by other effects, such as polymer diffusion. Additionally, the closer proximity of the glass transition temperature—which may have a dramatically broadened transition in thin films as opposed to bulk—may play a role here [47]. Lastly, at the earliest times (1–2 h), the poor contrast observed between the PI cylinders and the PS matrix via SEM may result from incomplete microphase separation—the PI may still be significantly mixed with the PS.

Polymer properties that measure a relevant time scale—such as diffusivity, viscosity, or here a correlation length—are often described by the William-Landel-Ferry (WLF) equation. Though semiempirical in derivation, the WLF equation captures the activatedlike nature of polymer properties in the vicinity of the glass transition temperature remarkably well. We use this here to create a master curve of the correlation length's time dependence (inset of Fig. 6). In order to create this master curve, we first calculate the relevant shift factors $a_T$ via the WLF equation:

$$\ln a_T = -c_1^0 (T - T_0)/(c_2^0 + T - T_0). \tag{3.1}$$

For PS ($T_g = 373$ K), the constants are $c_1^0 = 13.7$, $c_2^0 = 50.0$, and $T_0 = 373$ [48]. Additionally, an appropriate $T_g$ correction was applied as $T_g$ is depressed in the copolymer (as compared to pure PS) by the PI block. The shift factors for 413 K and 443 K are 18 and 797, respectively, and have been used to multiply the time scale of $\xi_2(t)$ for both temperatures. $\xi_2(t)$ for the two upper temperatures nicely maps onto a single line (with power law 1/4), but $\xi_2(t)$ for the lower temperature significantly diverges. This suggests that similar physics drives pattern coarsening for sufficiently ordered microdomains ($\xi_2 \gg 1$), but patterns with little or insufficient order (398 K, $\xi_2 \sim 1$) coarsen by other mechanisms.

Lastly, Lodge and co-workers [49] have measured the diffusivities of a PS-PI copolymer with similar molecular weights over a wide temperature range. Rescaling the time scale of $\xi_2$ by the diffusion constants we extrapolated does not shift the curves sufficiently such that they overlap in a convincing manner, perhaps because of a sufficiently dissimilar value of $\chi N$.

### C. Orientational defects—disclinations

To understand the driving force for the development of orientational order we studied the role of orientational topological defects [46,50,51]. Disclinations were identified by $\pi$ rotations of the director field along a closed path about a disclination core. We focused our attention on $\pm\frac{1}{2}$ disclinations (orientational or winding number defects that cannot be

removed through thermal fluctuations alone), the dominant orientational defects observed in our samples. Defects of other winding numbers were not observed with statistical significance.

We first measured the densities $\rho_{\pm}$ of $\pm\frac{1}{2}$ disclinations as a function of time and temperature from the same data sets shown in Fig. 3(a). Examples of both $+\frac{1}{2}$ and $-\frac{1}{2}$ disclinations are indicated in Fig. 3(b). We found that pattern coarsening reduces the density of defects $\rho_{\pm}$ as the correlation length $\xi_2$ increases. We plot the time dependence of $\rho_{+}^{-1/2}$, the average distance between disclination cores of the respective signs in Fig. 6(b). The magnitudes of $\rho_{+}^{-1/2}$ and $\rho_{-}^{-1/2}$ were virtually identical at all times and temperatures such that visual comparison is difficult as each data lies directly on top of the other, allowing only one to be visible. Here we only show $\rho_{+}^{-1/2}$. The interdisclination spacing can be seen to increase with the same power law as $\xi_2(t)$ shown in Fig. 6(a), indicating that $\rho \sim \xi_2^{-2}$. Note also that the magnitudes of $\xi_2$ and $\rho^{-1/2}$ are within a geometrical factor of each other (about 2), confirming that the orientational order of the sample is dominated by orientational defects. The similar values of $\rho_{+}^{-1/2}$ and $\rho_{-}^{-1/2}$ throughout the experiment suggest that the annihilation of disclinations of opposite sign is occurring, driving the growth of $\xi_2$. The low density of disclinations (typically of order unity in each SEM image at late times) contributes to the large error bars seen at late times.

The similarity of $\xi_2(t)$ and $\rho^{-1/2}(t)$ suggests that disclination annihilation dynamics are driving the increase in correlation length. We suggest then that the key to understanding the coarsening process of stripes lies in ascertaining the interaction and annilhilation of defects, which is the focus of subsequent sections.

### D. Correlation lengths perpendicular and parallel to microdomains

In addition to the azimuthally averaged correlation lengths, we measured the correlation lengths perpendicular ($\xi_{\perp}$) and parallel ($\xi_{\parallel}$) to the cylinder microdomain axis for the two higher annealing temperatures, which are shown in Fig. 6(a) as up and down triangles, respectively. The ratio of $\xi_{\perp}/\xi_{\parallel}$ remained approximately constant ($\sim 1.5$) during annealing at 443 K as the microdomain orientation influence was felt further perpendicular to the cylinder axis rather than parallel to the axis, as dictated by the energy cost of each type of distortion. As this measurement was made on a coarsening system, we do not interpret this ratio as an equilibrium property, but rather discuss the origin of this imbalance.

The higher value of $\xi_{\perp}$ with respect to $\xi_{\parallel}$ can be understood by examining four highly idealized distortions: molecular splay, molecular bend, and both plus and minus $\frac{1}{2}$ disclinations. We first consider the case restricted to molecular splay only. Figure 7(a) shows a block copolymer pattern which is analogous to that shown by a 2D smectic. Here we schematicize the chemical composition as light and dark regions [similar to Fig. 2(b)]; the molecular chains are shown as open and closed ellipses with an average orientation perpendicular to the interfaces. Since the distortion of the microdomain layers in Fig. 7(a) is classified as bend, this forces the distortion of the polymer chains to be molecular splay. Henceforth the distortion of splay and bend will always refer to the molecular distortion of the polymer chains. An example of the perpendicular and parallel directions with respect to the pattern is presented in Fig. 7(a). For this situation, both $\xi_{\perp}$ and $\xi_{\parallel}$ are long range (nonzero at distances comparable to the image size), but $g_{\parallel}(r)$ decays faster than $g_{\perp}(r)$. The microdomain orientation is parallel to the $\hat{x}$ axis at the crest or trough of the undulations. Proceeding along the $\hat{y}$ axis (perpendicular), the orientation of the microdomain remains parallel to the $\hat{x}$ axis and the correlation function remains high. Proceeding instead along the $\hat{x}$ axis (parallel), the orientation of the microdomain fluctuates, decreasing the correlation function. The regions of high corre-

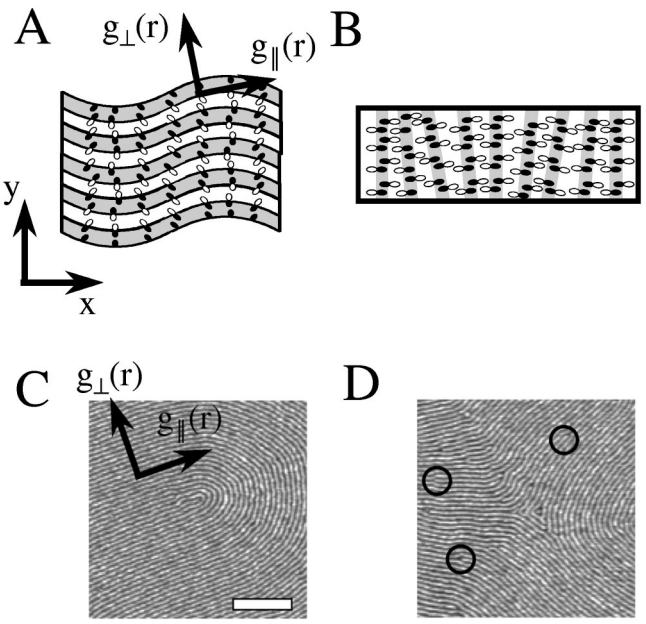


FIG. 7. Four configurations which we use to make arguments concerning correlation lengths perpendicular and parallel to the microdomain orientation. (a) Molecular splay. The light and dark regions correspond to the regions of each of the two polymer blocks. The polymer chains are drawn as open and closed ellipses with an average orientation perpendicular to the light-dark interfaces. An example of the parallel and perpendicular orientations at one location is given. In general, the parallel direction follows the region of light or dark and the perpendicular direction necessitates crossing into light then dark, etc. The microdomains undergo the distortion of bend, forcing the polymer chains into a configuration of molecular splay. This distortion, which is typically observed in smectics, results in $\xi_{\perp} > \xi_{\parallel}$. (b) Same as (a) but now with the polymer chains distorted into molecular bend. This configuration involves layer compression and expansion and is hence prohibitively energetically costly. However, if this configuration were to exist, it would result in $\xi_{\perp} < \xi_{\parallel}$. (c)–(d) Isolated disclinations [$+\frac{1}{2}$, panel (c); $-\frac{1}{2}$, panel (d)] with defect cores in image centers. An example of the perpendicular and parallel directions is indicated in panel (c). Note the higher density of dislocations (circled) in the strain fields of the $-\frac{1}{2}$ disclination in panel (d). For both disclinations, we measure $\xi_{\perp} > \xi_{\parallel}$. Bar=200 nm.

lation however lift $g_\perp(r)$ with respect to $g_\parallel(r)$. Hence the distortion of molecular splay produces a pattern where $\xi_\perp > \xi_\parallel$. At length scales much geater than the wavelength of the undulations, the correlation function intensity [whether $g_\perp(r)$ or $g_\parallel(r)$] is comparable.

We next consider the case of molecular bend, the complementary strain field to splay. We schematicize a possible microdomain configuration in Fig. 7(b), which consists exclusively of molecular bend (though the layers then exhibit splay). This distortion would result in a pattern where $\xi_\parallel > \xi_\perp$ as the microdomains are perfectly straight and correlated parallel to their orientation but not perpendicular to their orientation. In practice this configuration is never observed as it involves compression and dilation of the layer spacing, which is prohibitively energetically costly as it involves distortions of the polymer chain size rather than the reorientation associated with molecular splay. However, if this distortion took place, it would result in regions where $\xi_\perp < \xi_\parallel$.

Third, we consider the influence of a $+\frac{1}{2}$ disclination on the relative value of the correlation functions [Fig. 7(c)]. As was shown in the following section, the block copolymer microdomain pattern is dominated by disclinations, so their influence should be large. The energetic cost of molecular splay is relatively small as it only involves a reorientation of the molecules. However, the energetic cost of of layer compression and dilation (see earlier section) is relatively expensive as it necessitates molecular elongation or contraction, with an associated entropic penalty. This produces $+\frac{1}{2}$ disclination patterns which maintain a constant layer spacing due to the relatively high cost of molecular bend, but whose layers rotate by $\pi$ around the disclination core (exhibiting molecular splay) [52]. This pattern can be dislocation free while maintaining a constant layer spacing, but in practice several are typically seen near the disclination core (discussed further in Sec. III E). Measurements of $g_\perp(r)$ and $g_\parallel$ for Fig. 7(c) reveal that $\xi_\perp > \xi_\parallel$, which can be understood with a few arguments. Since the left half of panel (c) is uniform, there we must have $\xi_\perp \sim \xi_\parallel$ and we consider only the right half. In this configuration, the orientation of the microdomains is preserved as one travels radially from the center outwards ($\xi_\perp$) to the furthest extent, whereas the microdomain orientation changes as one follows a microdomain azimuthally around a disclination core ($\xi_\parallel$). This contributes to forcing $\xi_\perp$ to be greater than $\xi_\parallel$.

Fourth, we consider the influence of $-\frac{1}{2}$ disclinations on the relative values of the correlation functions [Fig. 7(d)]. In contrast to the $+\frac{1}{2}$ disclination in panel (c), where the microdomain or stripe spacing can be held constant throughout the strain field, a $-\frac{1}{2}$ disclination with this constraint cannot be constructed without either introducing dislocations or other defects. Evidence for this can be seen with the much higher density of dislocations in the strain field of the $-\frac{1}{2}$ disclination in Fig. 7(d). Measurements of $g_\perp(r)$ and $g_\parallel(r)$ reveal that $\xi_\perp > \xi_\parallel$, though the discrepancy should not be as large as for $+\frac{1}{2}$ disclinations as the strain field is less dependent on the elastic constants [52].

Therefore, of the four possible configurations, three configurations produce distortions where $\xi_\perp > \xi_\parallel$ (splay and $\pm\frac{1}{2}$ disclinations), and the configuration of bend does not contribute as it involves layer compression and dilation. It is the particular topology of a smectic which prohibits molecular bend from occurring, thereby increasing $\xi_\perp$ with respect to $\xi_\parallel$.

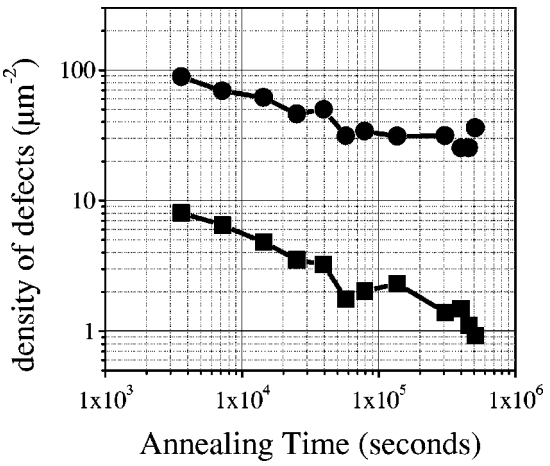


FIG. 8. Density of defects as a function of time for a sample annealed at 443 K on a carbon-coated substrate. Note that the density of elementary dislocations (upper curve) is at least an order of magnitude greater than the density of disclinations (lower curve) at all times. While annihilation of disclination pairs alone will increase the dislocation density, this is offset by both dislocation annihilation and quadrupole disclination annihilation.

### E. Dislocations

While nematic order breaks rotational symmetry and introduces the possibility of orientional disclinations, smectic order additionally breaks translational symmetry and introduces the possibility of edge dislocations. Though orientational order may develop after a quench through the annihilation of disclinations alone, the movement and annihilation of disclinations involves iterative steps which involve dislocations (further discussed and schematized in Sec. IV). Therefore, to try to understand the role of elementary dislocations in pattern coarsening, we investigated the density of dislocations ($\rho_\epsilon$) and their proximity to disclinations. Dislocations were computationally identified by the typical method of decomposition into tightly bound disclination pairs with a maximum cutoff distance between the cores of one repeat spacing $d$ [46]. An example of a dislocation is shown in the lower circle of Fig. 3(b). As there was no particular orientation to the sample, the orientation of the Burgers vector associated with the dislocation was generally ignored. We found that the dislocation density decreased during annealing with the disclination density. In Fig. 8 we plot the time dependence of both the $+\frac{1}{2}$ disclination density (lower data set, which has almost exactly the same magnitude as the $-\frac{1}{2}$ disclination density) and the dislocation density (upper data set) for samples that were annealed at 443 K. The density of dislocations decreased at a slightly slower rate than the density of disclinations, as shown in Fig. 8. Even though pairwise disclination annihilation alone produces dislocations (to be further discussed in Sec. IV C), here we see

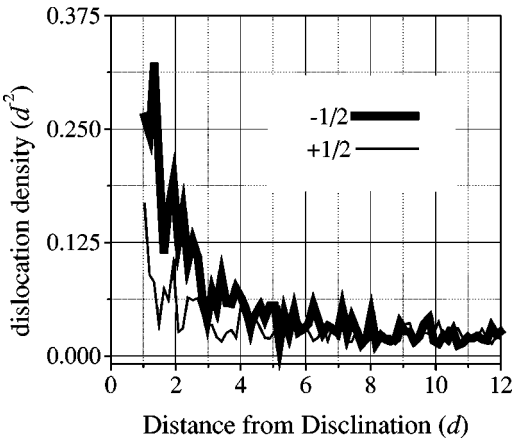


FIG. 9. The density of elementary dislocations $h(r)$ as a function of distance greater than repeat spacing $d$ from plus (narrow line) and minus (thick line) $\frac{1}{2}$ disclination cores. Dislocations are detected by decomposing them into bound disclinations of separation distance less than $d$. While there is a higher density of dislocations near both $\pm\frac{1}{2}$ disclination cores, note the higher density of dislocations near the $-\frac{1}{2}$ core than near the $\frac{1}{2}$ core. This higher density results from the hard constraint of a fixed layer spacing dictated by the perturbed radius of gyration of the polymer chain. While $+\frac{1}{2}$ disclinations may be constructed with a fixed layer spacing with only the lower energy strain associated with molecular splay, the formation of $-\frac{1}{2}$ disclinations necessarily involves layer spacing distortion, or alternatively, the insertion of a dislocation near the core, as shown in the right circle of Fig. 3(b).

a monotonic decrease in both the dislocation and disclination density, suggesting that other processes are occurring. Throughout the experiment, the dislocation density was about an order of magnitude higher than the disclination density.

We next examined the distribution of dislocation locations throughout the sample with the correlation function $h(r)$, which is essentially the *dislocation* density $\rho_\epsilon$ as a function of distance from a *disclination* core. We plot the density of dislocations $h(r)$ as a function of the distance away from $\pm\frac{1}{2}$ disclination cores in Fig. 9 in units normalized with the repeat spacing $d$. This data was obtained from a well-coarsened sample where $\xi_2 \sim 10d$. The pronounced rise in $h(r)$ for $r<4d$ shows that the dislocation density is highest near the core of either disclination of either sign, perhaps to relieve the local strain field of the disclination. In addition, Fig. 9 shows a higher density of dislocations near $-\frac{1}{2}$ disclination cores than near $+\frac{1}{2}$ disclination cores. This is due to a physical constraint; $+\frac{1}{2}$ disclinations can maintain a constant layer spacing about the core whereas $-\frac{1}{2}$ disclinations cannot. Dislocations near $-\frac{1}{2}$ disclinations can alleviate the higher strain about the core [see Fig. 7(d)]. At large distances, the dislocation density recovers to that of the sample average, and the difference between the dislocation density about disclinations of different signs disappears.

Integrating the dislocation density in Fig. 9 reveals that there are typically one to three dislocations trapped in the strain field of each disclination. Since Fig. 8 shows that there are around ten dislocations per disclination, this reveals that the remaining dislocations are not associated with a specific disclination, but rather are relatively free to move in response to strain introduced by disclination motion. Additionally, at times greater than $10^5$ s, Fig. 8 shows that the decrease of dislocation density slows while the disclination density continues to decrease. While dislocation annihilation can proceed with glide and climb, disclination movement in order to annihilate requires the collective motion of many dislocations as well.

## IV. OBSERVATIONS OF DEFECT ANNIHILATION

### A. Introduction

While scanning electron microscopy was employed for the most accurate measurements of the correlation lengths, the osmium tetroxide staining method necessary for effective imaging arrests all polymer dynamics. Therefore, to observe the dynamics of individual defects, which is the key to understanding the measured kinetic exponents, an alternative method of observing the microdomains was employed, which did not alter the chemical composition of the blocks. This was accomplished by taking advantage of the modulus difference between the two blocks and using tapping mode AFM to image the microdomain pattern. To minimize degradation during annealing, a hydrogenated diblock (denoted PS-PEP 5-13) was employed, which consisted of PS cylinders in a PEP matrix. Since PEP is a hydrogenated version of PI, PS-PEP 5-13 is akin to the morphological inverse of SI 30-11. The interfacial wetting blocks for PS-PEP copolymer thin films is currently being examined by dynamic secondary ion mass spectrometry and will be discussed in a later publication. Spin-coated samples were imaged at ambient temperature, annealed in air on a temperature-controlled heater stage mounted on the AFM [41], and then reimaged after cooling to examine the coarsening microdomain pattern. By repeating this cycle dozens of times and reimaging the same area, we observed the annihilation processes of disclinations. The annealing temperature was sufficiently low (368 K) and the annealing time was sufficiently short (hours) that an insignificant amount of degradation occurred. While, in principle, the time dependence of the correlation length could be measured via AFM as was done in the earlier section via SEM, in practice this was made impossible by the limited number of pixels per image (in the current AFM implementation) and image distortion introduced by piezohysteresis.

### B. Dislocation annihilation

The decrease in dislocation density $\rho_\epsilon$ shown in Fig. 8 indicates that pairs of dislocations of opposite orientation are attracting and annihilating (our focus here) or that they are being drawn into the core of disclinations. Elastic theory [51] finds that the strain energy $W_1$ of dislocations with Burgers vectors $\vec{b}_1$ and $\vec{b}_2$ is

$$W_1 = \frac{1}{4}\vec{b}_1 \cdot \vec{b}_2 \overline{B} \sqrt{\frac{\lambda}{\pi |z_1 - z_2|}} \exp\left( - \frac{(x_1 - x_2)^2}{4\lambda |z_1 - z_2|} \right). \tag{4.1}$$

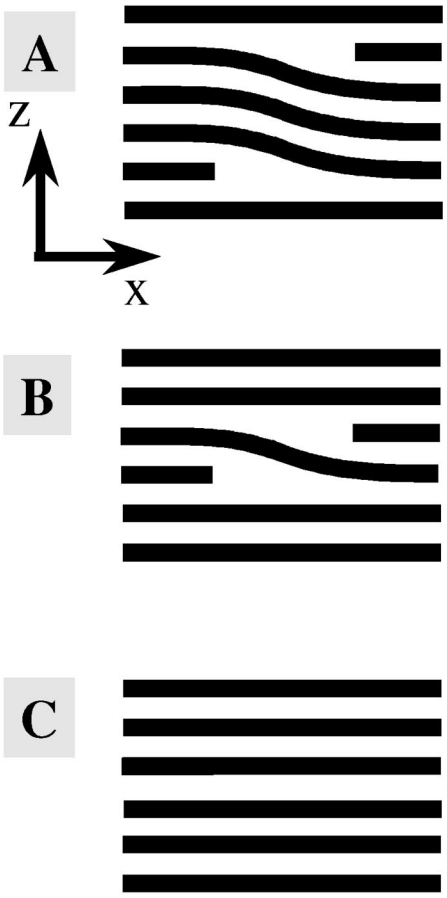


FIG. 10. Schematic of two dislocations of opposite Burgers vector annihilating. (a) The dislocations are separated by three layers. (b) The dislocations approach and are now separated by one layer. (c) Annihilation leaves a region free from topological defects.

An example of a schematicized dislocation pair is shown in Fig. 10; we use the $\hat{x}-\hat{z}$ axes as convention dictates where the structure is uniform in the $\hat{y}$ direction. The elastic constant $\lambda$ is defined as $\sqrt{K_1/\bar{B}}$, where $K_1$ is the splay elastic coefficient and $\bar{B}$ is the layer compressibility. This strain energy results in an attractive force $(F_x,F_z)$ for oppositely oriented dislocations as follows:

$$F_x=\frac{x\vec{b}_1\cdot\vec{b}_2\bar{B}}{2}\sqrt{\frac{\lambda}{\pi z}}\exp\left(-\frac{x^2}{4\lambda z}\right), \tag{4.2}$$

$$F_z=\frac{\vec{b}_1\cdot\vec{b}_2\bar{B}}{8}\exp\left(-\frac{x^2}{4\lambda z}\right)z^{-3/2}\sqrt{\left(\frac{\lambda}{\pi}\right)}\left(1-\frac{x^2}{2\lambda z}\right). \tag{4.3}$$

This force would pertain to the upper dislocation of Fig. 10(a) with the lower dislocation considered to be the origin. The interaction force that results from the above expression causes like-signed dislocations to repel and oppositely oriented dislocations to attract. However, the resulting motion causes the dislocations to follow a path which is longer than their initial separation distance. The annihilation process that results from this interaction reduces the total number of dislocations, as is schematicized in Fig. 10. Two oppositely oriented dislocations are shown attracting and annihilating, producing a pattern free of topological defects. The peculiarity of the interaction is evident in the change of sign of $F_z$ as one crosses the parabola of $x^2=2\lambda z$. Note also that the force drops off with $x$ exponentially—dislocations interact significantly weaker in a smectic than in hexatic crystals where dislocations interact exclusively via a power law. This is perhaps partly responsible for the lack of observed grain boundaries (clusters of dislocations) for this 2D smectic system.

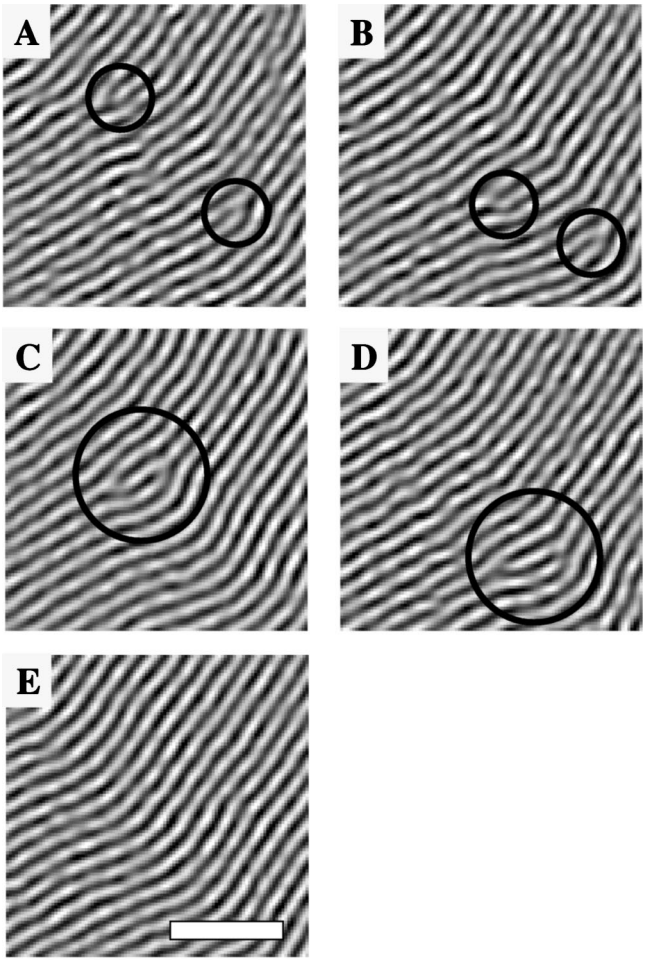


FIG. 11. AFM data showing two dislocations of opposite Burgers vector approaching and annihilating. (a) Dislocations separated by nine layers. (b) Separation distance between dislocations has been reduced to four layers. The two dislocations have additionally shifted their center of mass, presumably under the influence of defects out of the field of view. (c) The dislocation center again shifts and forms a bound pair. (d),(e) The bound pair annihilates. Bar $=150$ nm.

An example of this annihilation process in our system is shown in Fig. 11. This data comes from a relatively well-coarsened pattern annealed at 368 K where the total prior annealing time for the pattern shown in the first panel is 9 min. In panel (a) two oppositely oriented dislocations (circled) are shown where the distance between the indicated dislocations is shorter than the distance to the nearest topological defect. While the dominant forces on the two dislo-

cations may be their interacting strains, nearby defects (closest is about ten layers away) may also influence their trajectory. Subsequent panels show the pattern after annealing interludes of 1 min each. Panel (b) shows that the two dislocations have both translated and reduced their separation distance. In panel (c) the dislocation pair has again translated, reduced its separation distances, and appears to have formed a bound pair, which persists in panel (d). The pair disappears by panel (e), leaving a defect-free region.

There are several limitations to this observation which we acknowledge here. The coarseness of our movies prevents a measurement of the interaction force based upon the speed of defect motion. In addition, this coarseness limits our ability to examine the subtleties of dislocation motion—such as the direction of the interaction force as a function of location. Lastly, while we examine here dislocation pairs that may be so close enough that their motion is dominated by their own interaction forces, strain fields from nearby topological defects must play some role, as is evidenced in the movement of the center of mass of the dislocations from panel (a) to (b). Our lab is currently improving measurement methodology to increase our time resolution such that a better time sequence can be obtained.

### C. Annihilation of disclination dipole

Topological constraints dictate the favorability of various possible coarsening mechanisms involving orientational defects. We first discuss a disclination dipole and its related orientational strain energy. For nematic systems, the orientational strain of a disclination pair (such as shown in Fig. 12) dictates a logarithmic interaction potential:

$$E_{nem} = \pi k_1 k_2 K_1 \ln[r/d], \tag{4.4}$$

where $d$ is the repeat spacing, and $k_1$ and $k_2$ are the winding number for the defects (here $+\frac{1}{2}$ and $-\frac{1}{2}$, respectively). The attractive force then is

$$F_{nem} = 2\pi k_1 k_2 K_1 \frac{\hat{r}}{r}. \tag{4.5}$$

There is also a strain energy associated with compression and dilation of the layer spacing for such a configuration, but we focus here on the strain associated with the director field. This defect pair has an associated Burgers vector equal to twice the separation distance [53]. Hence the annihilation of a disclination pair produces a number of dislocations equal to the original Burgers vector divided by the layer spacing $d$. This is schematically represented in panels (a) and (b) of Fig. 12 and is also shown by the AFM data in panels (c) and (d). While dislocations shed in this process slowly annihilate with other oppositely oriented dislocations, this is less favorable than an alternative disclination annihilation process which produces few or no dislocations (which we describe in the following section). Consequently, we rarely observe this coarsening mechanism for disclinations pairs separated by more than a few layers, though we thoroughly searched our data for such annihilations. We suggest that the lack of such annihilations result from the topological constraint of dislocation production. This seems counterintuitive as there are ten times as many dislocations as disclinations (Fig. 8) and we observe their mobility to be high as compared to disclinations. However, a few dislocations of the appropriate orientation may be trapped in the strain fields of other defects, (see earlier section) mitigating their potential usefulness in assisting in the annihilation of a pair of disclinations.

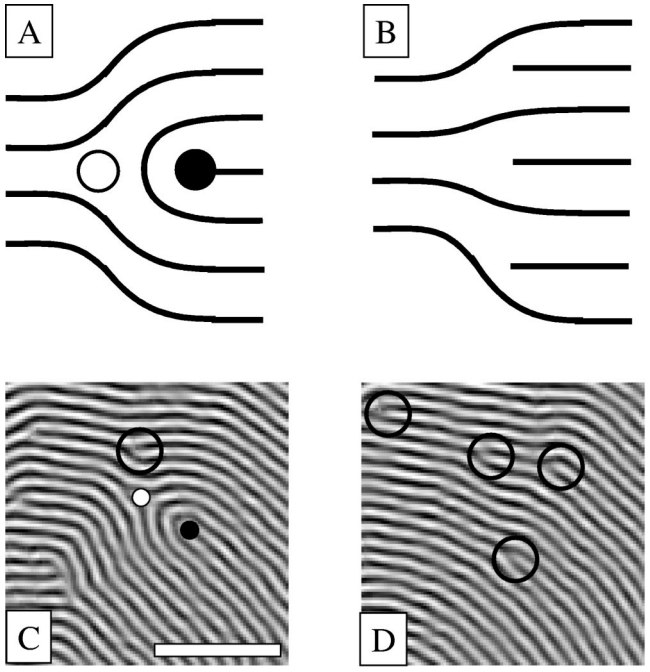


FIG. 12. Annihilation of disclination dipole, observed infrequently. (a) Schematic of a disclination dipole with Burgers vector $3d$, where the $+\frac{1}{2}$ disclination core is indicated with a closed circle, and the $-\frac{1}{2}$ disclination with an open circle. The strain fields cause the defects to annihilate, producing three dislocations after annihilation in panel (b). (c) AFM image of a disclination dipole [Burgers vector $6d$, cores indicated as in panel (a)], plus six additional dislocations, three each of the two orientations. One is circled. (d) The dipole has annihilated, and four dislocations (each circled), of the orientation corresponding to the dipole's original Burgers vector, remain in the field of view. Additional dislocations have moved out of the image area.

### D. Annihilation of disclination quadrupole

The annihilation of two disclination pairs (which we refer to as a quadrupole as it contains a total of four disclinations) allows the pattern to coarsen while both eliminating all orientational defects involved and minimizing the production of dislocations. In striking contrast to dipole annihilation, this mechanism of coarsening was observed during the entire coarsening process, from virtually the initial state of disorder to samples with correlation lengths on the order of dozens of repeat spacings. We try to establish this here by discussing two quadrupole annihilation events—one with an initial small separation distance $(5d)$ between disclinations and one with a large separation distance $(20d)$. Such quadrupole and tripole (further discussed in Sec. IV G) annihilation events

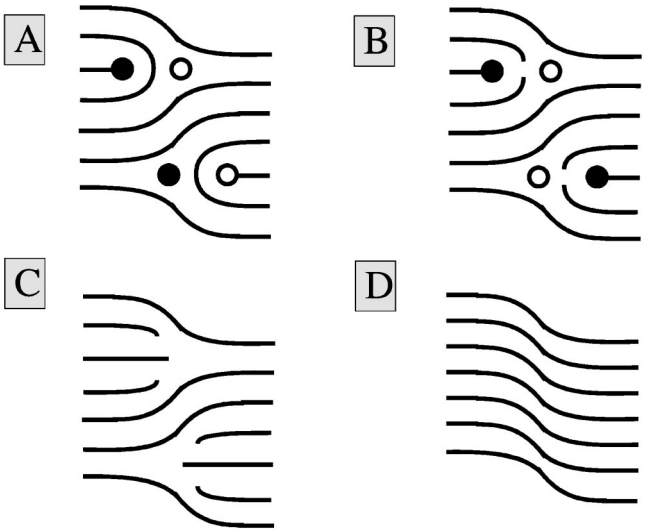


FIG. 13. Illustration of quadrupole configuration 1. This sequence shows two dipoles of disclinations in a configuration with zero net Burgers vector. The dark and light circles refer to the cores of plus and minus disclinations. Panels (a)–(d) show a possible annihilation process.

were observed approximately ten times as often as dipole events and were observed at all stages of the coarsening process (all length scales).

A quadrupole consists of two disclination pairs where each pair has an oppositely oriented Burgers vector of similar magnitude. One possible quadrupole configuration is shown schematically in Fig. 13(a). The net Burgers vector for this cluster of four disclinations is zero, so its annihilation is not topologically hindered like that of a disclination dipole alone. The associated strain fields of the defects induce the four disclinations to attract, leaving a region free of topological defects [panels (b)–(d)], albeit with a screened interaction.

The annihilation process schematicized in Fig. 13 is observed in the AFM images shown in Fig. 14. Panel (a) shows four disclinations in a configuration reminiscent of two dipoles. The separation distance between the positive disclinations is eight layers after annealing for 6 min at 368 K. After 2 min of annealing further, panel (b) shows that this distance has been reduced to seven layers, and in panel (c) (another 3 min), 5.5 layers. The nonintegral separation distance results from the disparate cores of the positive disclinations, the left plus disclination consists of a cylinder (lighter) in panel (b); the right consists of the matrix (dark). Distances are not counted in absolute numbers but in the number of light-dark oscillations one encounters in traversing the distance between cores. A minimal Burgers vector construction in panel (c) reveals that there is a surplus of one layer on the right hand side. Similar constructions for panels (a) and (b) reveal an extra layer on the left hand side of the image—dislocations can diffuse in and out of the field of view (especially pertinent for longer anneal times between observations), negating the Burgers vector conservation laws. Subsequent panels occur after 1-min annealing steps, minimizing this effect. Panel (d) (1-min annealing further) shows

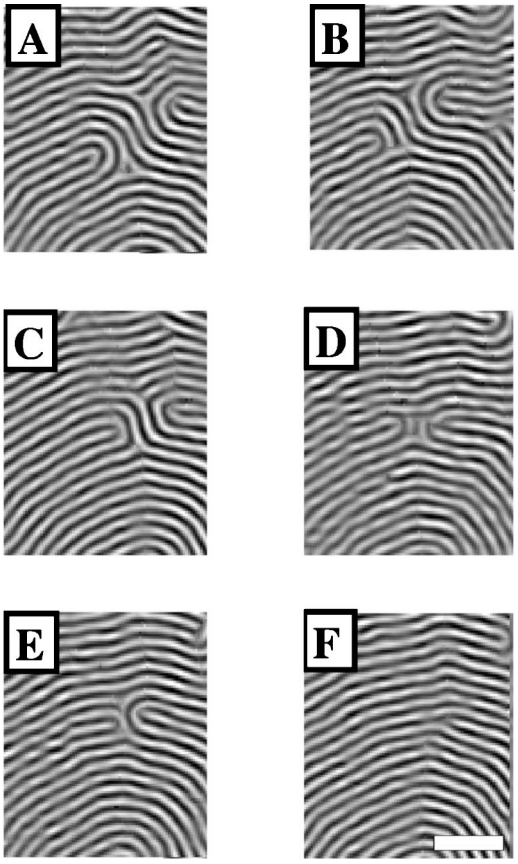


FIG. 14. AFM images taken from a sequence showing annihilation of disclination quadrupole which is initially separated by only eight layers. (a) After annealing for 6 min at 368 K, the spacing between $+\frac{1}{2}$ disclinations is eight layers. (b) After annealing 2 min further, the separation distance has been reduced to seven layers. (c) After annealing of 3 min further, the separation distance is 5.5 layers. A Burgers vector construction reveals that there is a surplus of one layer on the right hand side. Subsequent images are shown with 1-min intervals. (d) The separation distance is 3.5 layers. (e) The separation distance is three layers. (f) All orientational defects have annihilated, leaving the requisite dislocation on the right hand side. Bar=150 nm.

that the separation distance has been reduced to 4.5 layers, and in panel (e) (+1 min) three layers. Finally in panel (f) (+1 min), the orientational topological defects have completely vanished, leaving the requisite single dislocation which simply conserves the Burgers vector.

We now consider another typical quadrupole annihilation but with a larger initial separation distance. We schematicize this larger sized annihilation process with Fig. 15 and present the AFM images in Fig. 16. While Figs. 15 and 13 are topologically identical, Fig. 15 perhaps more effectively captures the subtleties of the larger-sized quadrupole annihilation. The representative panels of Fig. 16 were taken from a sequence of AFM images tracking the coarsening process at 368 K. Four well-separated disclinations (two $+\frac{1}{2}$ disclinations and two $-\frac{1}{2}$ disclinations) can be seen in Fig. 16(a) after annealing for 21 min. The separation between positive disclination cores is $37\pm1$ layers and the separation between negative disclination cores is $15\pm1$ layers. The uncertainty reflects

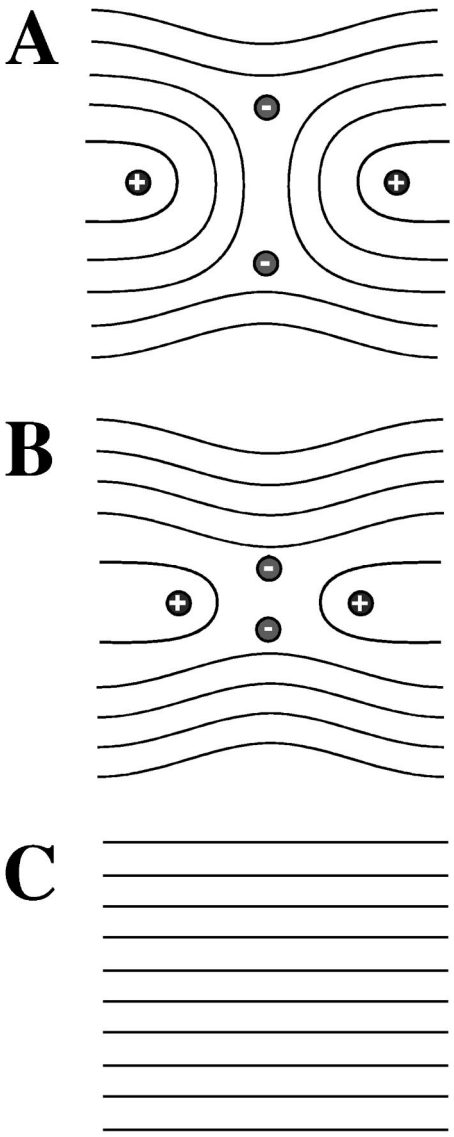


FIG. 15. Schematic of the quadrupole mechanism which dominates the coarsening process. (a) A symmetric quadrupole having net Burgers vector zero, with $+\frac{1}{2}$ disclinations indicated with a "+" and $-\frac{1}{2}$ with a "−." (b) Same quadrupole after disclination motion where the average separation distance is reduced. (c) After annihilation, no topological defects exist, as no disclinations remain and no dislocations are produced. However, for a quadrupole having a nonzero Burgers vector, the requisite number of dislocations would be created during annihilation.

the difficulty in locating the disclination core center. After annealing for 13 min further [Fig. 16(b)], the spacings decrease to $17\pm1$ layers and $12\pm1$ layers, respectively. As there are many dislocations also present nearby, the net Burgers vector for the disclination quadrupole is quite dependent on the precise path one choses to encircle it. However, a typical closed path which encircles the disclinations, passing a few layer spacings away from their cores, reveals that there is a surplus of approximately five layers on the left in panel (b). Panels (c)–(f) are obtained sequentially with 1-min intervals of annealing. The disclination cores continue to attract until panel (e), at which time all evidence of the disclinations has disappeared, and a small group of like-charged dislocations remains after their annihilation. Note that the number and Burgers vector of these dislocations is largely in agreement with the five excess layers associated with the quadrupole in panel (b). While there is reasonable correspondence between the quadrupole Burgers vector and the number and sign of dislocations produced after annihilation, the poor time resolution of this sequence of stills and the high mobility of dislocations limits our ability to absolutely associate particular dislocations with the quadrupole annihilation. Figure 16(f) shows these like-charged dislocations as they repel and separate from one another, consistent with Eqs. (4.2) and (4.3).

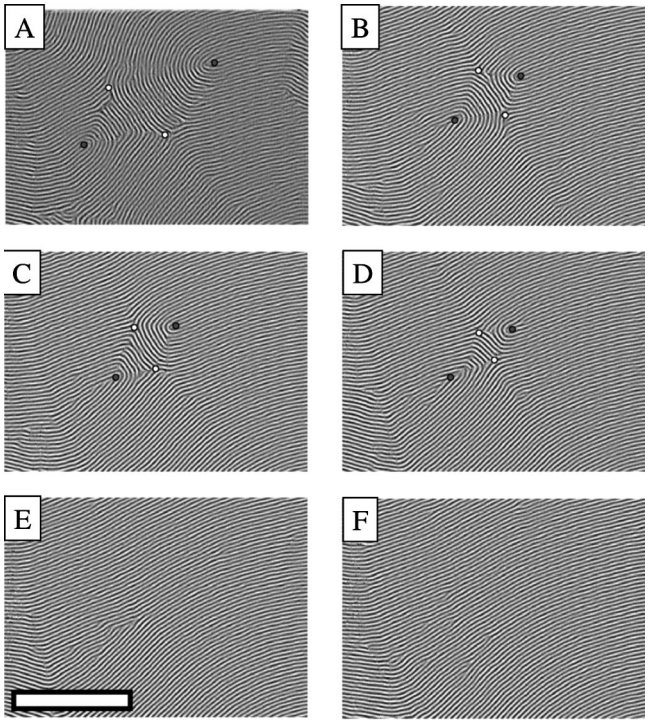


FIG. 16. AFM images taken from a sequence showing annihilation of a disclination quadrupole, which is initially well separated during annealing at 368 K. Cores are indicated by filled circles. (a) After 21 min of annealing, the disclinations are widely separated, and there are other topological defects in the field of view. (b) After 13 min of annealing further, the disclination spacing has decreased roughly twofold; the quadrupole has a Burgers vector of about $5d$, depending on the exact location of the chosen path. Subsequent panels are obtained with 1-min intervals of annealing, for which the spacing continues to decrease until panel (e), where the quadrupole has annihilated, leaving a cluster of about four dislocations. This cluster can best be seen by viewing the image at an oblique angle parallel to the stripes. (f) Dislocations repel and separate. Bar=300 nm.

### E. Quantitative analysis of quadrupole annihilation

The time dependence of annihilating disclinations allows one to test the consistency of the measured 1/4 power law with defect motion. We apply this to Fig. 16 and plot the average separation distance raised to the fourth power between like-signed disclinations in Fig. 17. The earliest time

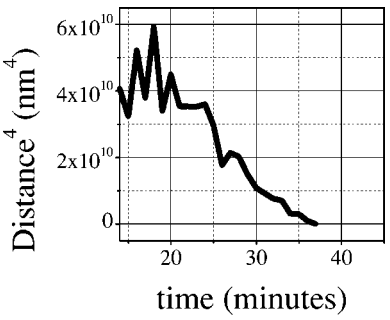


FIG. 17. We plot the average spacing between disclinations raised to the fourth power as a function of time for the images shown in Fig. 16. A straight line would indicate consistency with a $t^{1/4}$ power law.

is chosen as the point at which the strain field bounded by the quadrupole contains no other disclinations. Dislocations, however, were identified at all times. By plotting the distance between defects raised to the fourth power, we examine the consistency with a 1/4 power law for their interdefect spacing, which would give rise to the power law with the same exponent for $\xi_2(t)$. The average separation distance can be seen to decrease at an initially slow rate, which rapidly increases and becomes somewhat linear. A straight line would indicate consistency with a 1/4 power law, and the agreement here is surprisingly good. Though the limited range of distance (factor of 2–3 in distance) reduces our confidence in any measured exponents, it is inconsistent with a 1/2 power law as one might expect for a disclination pair for a nematic system, hence supporting the idea of topologically constrained disclination motion giving rise to a low exponent.

### F. Interaction of dislocations with disclinations

While the number of dislocations is reduced by annihilation events as discussed above, disclinations can also act as a source or drain for dislocations. In doing so, disclinations facilitate their motion in response to strain fields. An example of this is schematicized in Fig. 18. These four panels show that a dislocation can facilitate the motion of a disclination. Panels (a)–(d) show the motion of a dislocation towards the lower part of the diagram, which in turns moves the disclination core towards the upper part of the diagram. When the panels are observed as moving forward chronologically, the disclination acts a source for dislocations. However, the disclination acts as a drain if one views the panel in reverse order.

We present supporting data in Fig. 19 taken from a time sequence of AFM images. The core of the disclination is initially light, then dark, then light. This alternation of the disclinations core was seen for all disclinations examined. These changes in the disclination core may reflect the movement of the disclination by dislocation absorption or emission, but our time resolution here is not sufficient to resolve this motion. Positive disclination cores were examined statistically throughout the coarsening experiment, but no preference for light or dark (cylinder or matrix) was seen. This is surprising as there is an asymmetry between the two [50].

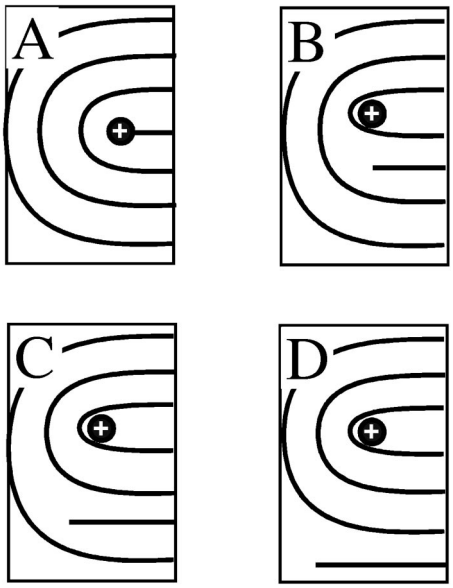


FIG. 18. Mechanism for moving a $+\frac{1}{2}$ disclination up by moving a dislocation down. Dark lines denote cylinders. (a) Disclination only centered in panel, core identified by "+." (b) By cutting one innermost dark line and reconnecting with center line we have created an extra terminated cylinder and the disclination core has moved up. (c) Dislocation moves down. (d) Dislocation moves further down and away from disclination strain field.

### G. Partial annihilation of disclination tripole

While annihilation events involving two disclinations were rarely observed, events involving three disclinations were frequently seen. For the case of three disclinations where one charge is dissimilar, two can annihilate and the third can act as a sink and absorb disclinations as shown earlier. The upper portion of Figs. 20(a,b) shows an illustra-

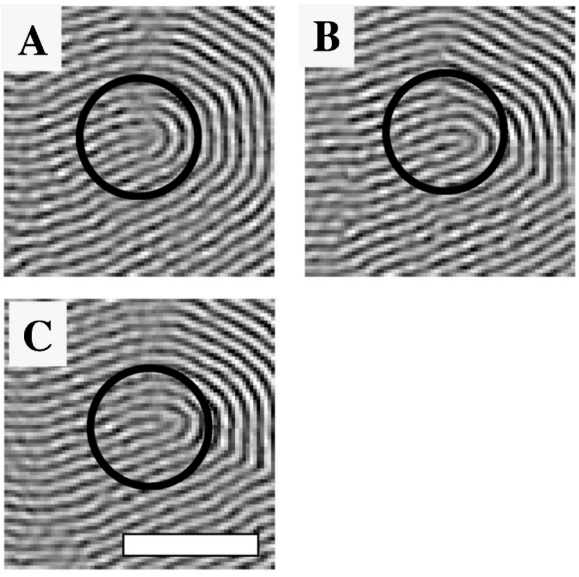


FIG. 19. Time sequence of AFM images where the disclination core (circled) alternates between light, dark, and light. Almost all disclination cores were observed to fluctuate in this manner. Bar =200 nm.

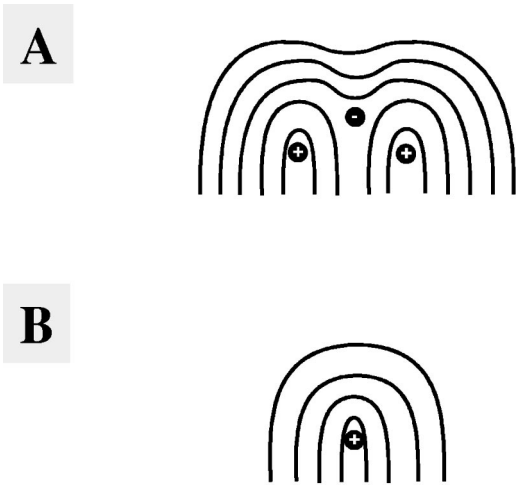


FIG. 20. Tripole going to monopole. (a) Schematic showing three disclinations (two plus, one minus). Note that the net disclination charge is $+\frac{1}{2}$. (b) Final state after a plus and minus disclination have annihilated, leaving a solitary $+\frac{1}{2}$ disclination.

tion of three disclinations, two plus and one minus, transforming into one dislocation (lower part). The single positive disclination is created, conserving disclination charge. The dislocations produced by this process are absorbed in the remaining disclination, as shown earlier.

Figure 21 shows a second tripole annihilation process with enough time resolution such that some dislocation motion can be observed. Panel (a) shows three disclinations (two plus, one minus) contained within an oval after annealing at 368 K for 10 min. The size of the upper disclination suggests that it will be of larger influence and we identify the lower two as a bound pair of sorts. Further annealing for 2 min more [panel (b)] changes the lower two disclinations into several dislocations, or alternatively, into a sort of grain boundary. Panel (c), obtained after annealing for 3 min further, is more straightforward to interpret. The lower circle shows that the Burgers vector for the bound pair has been reduced, necessarily involving the shedding of dislocations. Several of these dislocations are indicated by the arrow, which we suggest are being absorbed by the larger upper disclination (circled). Panels (d) (+ 2 min)–(e) (+3 min) show the almost complete absorption of the balance of dislocations into the upper disclinations.

While the coarseness of our time resolution prevents us from tracking dislocations with the preferred level of precision, we argue here that this is an example of the type of dislocation motion that is necessary for disclinations to annihilate or translate.

## V. UNDERSTANDING THE DYNAMICS

### A. Our model

We now discuss the origin of the measured kinetic exponents using the above mechanism of coarsening as a guide. The essential topological constraint on the evolution of these stripe patterns is that disclination motion requires the production or absorption of dislocations, lowering the kinetic exponent from that observed in nematic systems (1/2)

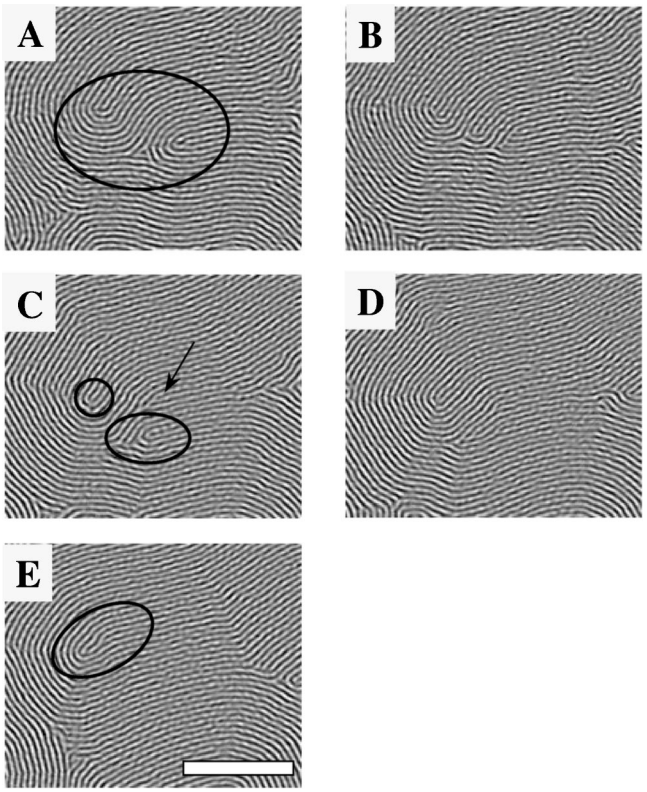


FIG. 21. AFM data of tripole of three disclinations merging to form a monopole. (a) Three disclinations (two plus, one minus) are present in the oval. The two lower disclinations form a bound pair of sorts with a separation distance of five layers. (b) An intermediate state where the topological defects are not easily identifiable. (c) The topological defects are once again easily identifiable. The upper circle shows the $+\frac{1}{2}$ disclination, an arrow indicates two dislocations, and the lower oval shows the ''bound'' state of a plus and minus disclination pair. Note that their separation distance is smaller (about three to four layers) than in panel (a). The dislocations indicated here may be in the process of ''exchange'' from the lower pair of bound disclinations with the upper disclination. (d) The lower two disclinations have shed dislocations which move towards the upper disclination. (e) The upper disclination absorbs most of the remaining dislocations. Bar=200 nm.

[54,55]. Pattern coarsening will progress if the free energy is being reduced. Processes involving the creation of fewer dislocations are favored since each costs a core energy. Thus the annihilation of a pair of disclinations alone is rarely seen as this requires transforming the Burgers vector into dislocations. Multidisclination annihilations are more favorable because a third disclination can act as a source or sink of dislocations, relieving the topological constraint and allowing an oppositely charged pair of disclinations to approach and annihilate. Alternatively, a set of four disclinations can be arranged that they have no net Burgers vector (Fig. 15); these four may then mutually annihilate without a net production of dislocations. Only about one-half of all disclination annihilations could be characterized in our experiments; of these, almost all involved are tripoles or quadrupoles, leading us to consider associated annihilation mechanisms to motivate the measured kinetic exponents.

For concreteness consider a disclination quadrupole where the average separations are $r$. This model applies equally to multidisclination annihilation events. Oppositely charged disclinations attract with a potential varying as $\ln(r)$, where $r$ is the distance between them. This produces forces on the disclinations varying as $1/r$. However, the disclinations cannot simply move in response to these forces, due to the topological constraint. Let us assume that the elementary step that allows a pair of $\pm\frac{1}{2}$ disclinations to move together by one layer requires the motion of a dislocation from one disclination pair to another. Thus a dislocation must move a distance $r$ in order for the disclinations to move only one unit. The resulting decrease in the free energy of the disclination strain field is of order $\Delta E \sim 1/r$. The force $f$ driving the dislocation's motion is the energy change divided by the distance traveled $r$, $f \sim \Delta E/r \sim 1/r^2$ (naively). If we assume that the dislocation motion is viscous with a speed proportional to force, the dislocation's speed is $v \sim 1/r^2$. Since the dislocation has to travel a distance $r$, the time for this process (whose net result is only one unit of disclination motion $dr \sim 1$) is $dt \sim r/v \sim r^3$. Thus the disclinations move towards one another as $-dr/dt \sim 1/r^3$, yielding $r \sim (t_f - t)^{1/4}$, where $t_f$ is the time when they annihilate. This scenario suggests that the typical spacing between the remaining disclinations at time $t$ grows as $\xi(t) \sim t^{1/4}$, consistent with our measured exponent in Fig. 6(a).

Finally, it is worth noting that the interaction force of Coulombic dipoles interacts with a $1/r^3$ force in 2D as well, yielding a $t^{1/4}$ power law as well. In some sense, the kinetics here can be thought of as the interactions of charged particles in 2D where the driving force is their Coulombic interaction subject to the constraint that only quadrupoles can annihilate.

### B. Comparison to simulations and previous results

Though there are few nondissipative systems appropriate for studying the pattern coarsening of stripes, dissipative systems such as the rolls observed in Rayleigh-Benard convection cells have been extensively investigated. Unfortunately, the sample cell size is experimentally limited to less than several hundred ''rolls,'' precluding their use as a model system for the study of coarsening exponents. Edge effects play a large role in small systems and collections of well-spaced interacting disclinations (such as those studied here) are difficult to generate. However, other properties of driven convection patterns have been extensively studied as a function of quench depth and as a function of time [56]. Dislocations have been studied by nucleation and an evolution to grain boundaries has been reported [57]. Similarly driven nematic systems exhibit a roll periodicity for which observations concerning dislocation strain fields and their motion have been made though there has been little or no work concerning the annihilation of orientational defects [58,59]. Lastly, garnet films are also experimentally accessible and produce patterns of high contrast, but the observed coarsening primarily results from the adoption of an equilibrium repeat spacing resulting from a temperature or field jump. Little temporal coarsening has been reported where the repeat spacing is held constant [6,60,61]. In all of these studies, there has been little or no work on the coarsening dynamics of disclinations. However, recent work on convection in a zig zag morphology has yielded a consistent 1/4 exponent [62].

While experimental work on the the coarsening kinetics of stripes is limited as described above, there have been numerous simulations during the past decade which bypass edge effects with periodic boundary conditions. Though earlier simulations focused on striped systems well described by the nonconserved dynamics of Rayleigh-Benard cells [63–68] recent work has established the applicability of this work to smectic or diblock copolymer systems where the dynamics are governed by a conserved density field [69]. Simulations predict that the orientational correlation length grows with a fractional power law with an exponent of 0.25 for both dissipative Swift-Hohenberg simulations and the conserved dynamics of diblock copolymer systems in the absence of noise. The addition of a small amount of noise (an analogy is made to increasing the temperature) was consistently shown to increase the measured exponents, with reported values up to 0.3. A large amount of noise has been shown to decrease the measured exponent [65]. Hence our measurement of the kinetic exponent for the orientational correlation length (Fig. 6) of 0.25 is consistent with the the large body of literature on striped systems.

While simulations have shed insight onto pattern coarsening kinetics, there has been almost no discussion or analysis (with the notable exception of Hou and Goldenfeld [63]) of the particular topology of striped systems and how this may physically motivate the measured exponents. For example, little attention has been paid to the often-observed dislocations or disclinations. The large role of the latter in the coarsening of nematic systems would suggest that topological defects should play a similarly large role in smectic coarsening [55]. To our knowledge, there have been few studies of the motion of individual disclinations or their annihilation processes. Researchers studying coarsening in other systems, such as the $x$-$y$ model, have made considerable progress by choosing their initial configurations to consist of two or four defects [54]. Similar artificial configurations—such as a quadrupole of disclinations—could be studied for a smectic-like system to gain insight into screened defect interactions. This would simply require that the initial conditions be switched from a random field to a specifically tailored disclination configuration. While this has not been done for stripes, the temporal evolution of defect configurations in hexagonally symmetric patterns have been investigated [70,71]. These researchers have yielded insight into the evolution of grain boundaries from starting configurations of disclination clusters. With similarly seeded configurations for stripes, we suggest that great progress could be made as to the interaction of disclinations and dislocations.

An additional application of simulations would be for increasing our time resolution. The current coarseness of our time resolution prevents us from observing dislocation motion with the desired level of detail. For example, we cannot measure the relative velocities of glide vs climb. For smectic systems, climb is (surprisingly) predicted to be more favorable [72]. The finer time resolution of simulations may allow for a more complete picture of defect motion.

## VI. RESULTS—QUASISTATIC PROPERTIES OF STRAIN FIELDS IN DEFECT-FREE GRAINS AND NEAR ISOLATED DISCLINATIONS OR DISLOCATIONS

### A. Introduction

Though the previous sections show that this system is far from equilibrium, studies of the well-ordered state can be used to extrapolate the elastic constants of the system. To this end we examine large grains of virtually defect-free regions and also the strain fields of relatively isolated topological defects. The measured orientational and translational correlation functions provide evidence that our system is consistent with the predictions for a 2D smectic system. We show that in defect-free regions translational order is destroyed by variation in the orientation field rather than by dislocations. The strain fields of disclinations are used to measure the ratio of elastic constants $K_3/K_1$, where $K_3$ reflects the energetic cost of molecular bend and $K_1$ reflects that of molecular splay. The strain fields of dislocations are used to measure an upper bound on the ratio of $K_3/\overline{B}$ where $\overline{B}$ is the layer compressibility at fixed density (not the bulk compressibility).

### B. Grain

At finite temperature, theory dictates that a 2D smectic has quasi-long-range orientational order and short-range translational order [2]. While translational order is typically destroyed by dislocations in three-dimensional crystals, defect-free elastic distortions alone are predicted to destroy translational order for a 2D smectic. To test the consistency of our system with these predictions, we studied sufficiently well-coarsened samples such that micron-sized grains could be readily identified. By choosing a grain with few dislocations we can test whether translational order is destroyed at length scales shorter than the separation distance of dislocations. This was accomplished by calculating the correlations $g_2(r)$ and $g_G(r)$ for a well-ordered region.

In order to fully and most convincingly ascertain the nature of order in the sample, one must examine samples with a single, well-oriented grain, with subsequent experiments showing that any correlation functions measured for this sample were largely independent of the size of the sample. While the small grain size of our system makes this impossible, we believe the trends in our data are meaningful as the many grains and disclinations (with different annealing histories) have yielded consistent results.

A typical grain from our well-annealed samples is shown in Fig. 22, where the long-range orientational order is evident from the largely horizontal orientation of the cylinders throughout the image. The translational order, however, appears to be destroyed by the softness of the system to undulations in the microdomain orientation field; the cylinders are not straight. The orientational deformations shown here are quasistatic and unlikely to be thermal fluctuations—they are presumably imposed by history, distant defects, or other imperfections. Two dislocations (circled) can be seen in the entire field of view, but disclinations are entirely absent from the image, preserving the long-range orientational order. This is made more quantitative with the azimuthally averaged correlation functions $g_2(r)$ and $g_G(r)$, which are plotted in Fig. 23(a). The orientational correlation function decays from 1.0 to about 0.8 at a distance comparable to the image size, whereas the translational correlation function decays to $e^{-1}$ within a few repeat spacings ($\xi_G \sim 3d$) and then fluctuates about zero. Since this latter decay distance is much shorter than the distance between dislocations, we argue that orientational distortions have destroyed long-range order in agreement with predictions for a 2D smectic.

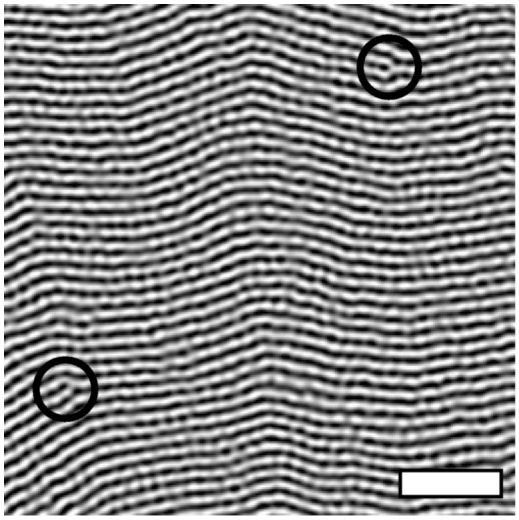

FIG. 22. SEM image of the relatively well-ordered grain of PS-PI 30-11. Two dislocations are circled. While this region exhibits orientational order, translational order is destroyed within a few repeat spacings by the orientational undulations of the microdomains (see Fig. 23). Bar=200 nm.

A semianalytical and somewhat geometrical argument can show the influence of the orientational distortions on translational order. We show this by first calculating the azimuthally averaged angle-angle correlation function $\overline{\theta^2}(r) = \langle [\theta(0) - \theta(r)]^2 \rangle$ [Fig. 23(b)]. A careful inspection of panels (a) and (b) of Fig. 23 shows that $\overline{\theta^2}(r)$ can be mapped onto $g_2(r)$ by multiplying the former by $\approx 3$ and subtracting it from 1. A small angle expansion of $g_2(r)$ is useful to illustrate why:

$$g_2(r) = \langle e^{2i(\theta(0) - \theta(r))} \rangle \sim 1 + 2i[\theta(0) - \theta(r)] - 4[\theta(0) - \theta(r)]^2 \cdots . \quad (6.1)$$

The second term [linear in $\theta(0) - \theta(r)$] in the above equation averages to zero, leaving only the quadratic term with the unity offset. This implies that $g_2(r) \sim 1 - 4\overline{\theta^2}(r)$. An inspection of Fig. 23(c) reveals this to be approximately correct $-g_2(r)$ decreases as $\overline{\theta^2}(r)$ inceases, and vice versa. The correlation function $g_2(r)$ decays to about 0.8 at 30 repeat spacings, whereas $1 - \theta^2(r)$ is around 0.68 at the same distance. The slight difference in magnitudes is most likely due to higher order terms in the expansion.

The translational correlation length corresponds to a distance over which the cylinder layers become displaced by $d/4$, or out of phase by $\pi/2$, from that of the cylinder at the

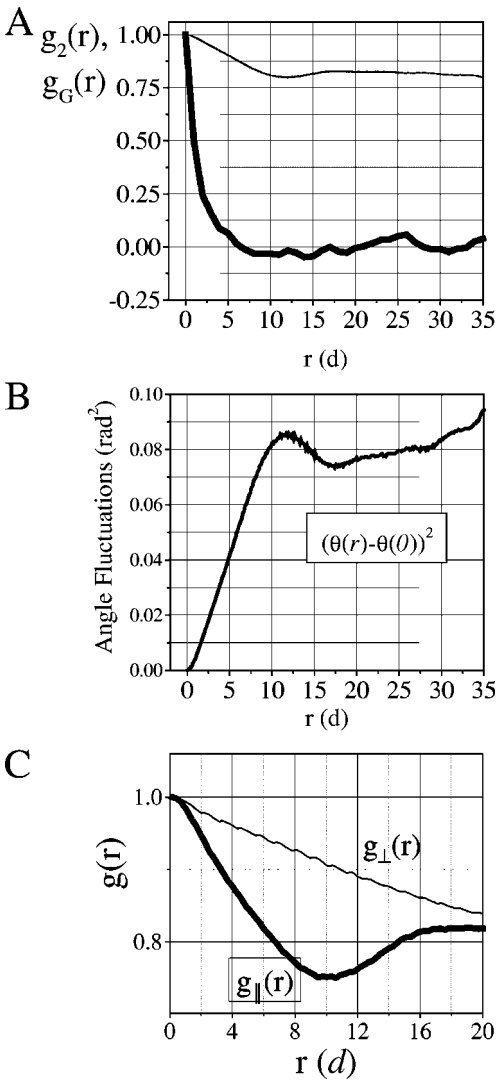


FIG. 23. (a) Orientational $g_2(r)$ (thin line) and translational $g_G(r)$ (thick line) correlation functions for a grain of well-oriented microdomains (previous figure). Note the orientational order remains nonzero at a distance of $r=35d$ (where $d$ is the repeat spacing of the cylinders), comparable to the image size. However, the translational order has decreased to the noise level at a distance of $r=5d$. This demonstration of long-range orientational order with short-range translational order is consistent with the theoretical understanding of a 2D smectic. (b) Orientational fluctuations for the same data. The apparent mirror symmetry between panels (a) and (b) is consistent with destruction of translational order with microdomain orientation undulations. (c) Orientational correlation functions for correlation pairs perpendicular and parallel to the microdomains. Note that $g_{\|}(r)$ decays more rapidly with distance than $g_{\perp}(r)$ for this single grain. This is also seen for multiple grains, as is shown with $\xi_{\perp}$ and $\xi_{\|}$ in Fig. 6(a). The ripples on $g_{\perp}(r)$ occur with a separation distance corresponding to the repeat spacing and are an artifact of image processing, they can be removed with further smoothing.

starting point. Given $\overline{\theta^2}(r)$, we can solve for the distance $l$ necessary to travel along a cylinder axis in order for the orientational deformations to displace the cylinder center by $d/4$. If we solve $\theta(r)r\sim d/4$, where $\theta(r)$ is determined from $\theta^2(r)$, we obtain $r\sim 3d$. This suggests that the orientational deformations alone produce a translational correlation length of $3d$, consistent with the rapid decay of the translational correlation function for a 2D smectic at nonzero temperature.

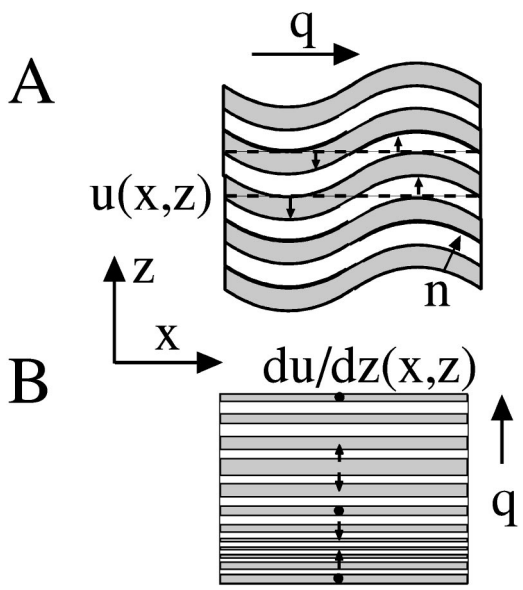


FIG. 24. Distortional fields in a smectic crystal as produced by the displacement field $u(x,z)=u_0\sin(\vec{q}\cdot\vec{x})$. (a) Here $\vec{q}$ is parallel to the $\hat{x}$ direction. The layers undulate with amplitude $u_0$ and wavelength $2\pi/q$, the latter being equal in width to this panel. The local magnitude of $u(x,z)$ is indicated by arrows in three places, which originate at the dashed lines (where the layers would reside if unperturbed) and terminate at a distance determined by the magnitude and sign of the local value of $u$. The direction of the unit normal $\hat{n}$ is indicated in one location. (b) Compression and dilation of layers is produced by rotating $\vec{q}$ to be normal to the layers and parallel to $\hat{z}$. We indicate the magnitude of the compression or dilation with arrows in the center. The layers are uniform in the $\hat{x}$ direction. The filled circles indicate regions where the layers are unperturbed and the wavelength of the perturbation is equal to the height of this panel. The two opposing arrows indicate a region of dilation ($\partial u/\partial z>0$) and the two self-pointing arrows indicate a region of compression ($\partial u/\partial z<0$).

### C. Fixed repeat spacing

A casual inspection of Fig. 22(a) reveals that this system exhibits a narrow distribution of layer spacings with long wavelength undulations in the layer orientations. We show here that this results from the distortional energy associated with molecular splay ($K_1$) being $10^3$ lower than that for layer compressibility ($\overline{B}$) [16]. We start with the two-constant phenomenological equation for the relative energies of molecular splay and layer compressibility. For layers in the $\hat{x}-\hat{y}$ plane, with a unit normal $\vec{n}$ in the $\hat{z}$ direction (Fig. 24), the energy $W$ can be written as

$$W=\int\left[\frac{1}{2}K_1(\vec{\nabla}\cdot\vec{n})^2+\frac{1}{2}\overline{B}\left(\frac{\partial u}{\partial z}\right)^2\right]\partial x\,\partial z, \qquad (6.2)$$

where $u(x,z)$ is the spatially dependent distance by which the layers are displaced from their undistorted configuration. The pattern is assumed to be uniform in the $\hat{y}$ direction. This equation can be cast in a more useful form for our purposes, which depends only on $u(x,z)$ by modifying the splay curvature term:

$$W=\int\left[\frac{1}{2}K_1\left(\frac{\partial^2 u}{\partial x^2}\right)^2+\frac{1}{2}\overline{B}\left(\frac{\partial u}{\partial z}\right)^2\right]\partial x\,\partial z. \tag{6.3}$$

We may calculate the ratio of energy densities by considering two sinusoidal perturbations to a defect-free orientational field with amplitudes $u_0$ and wave numbers $\vec{q}$. Parallel to the cylinder axis, the microdomains meander with long wavelength undulations, which maintain a constant repeat spacing, lowering $\xi_\parallel$ with respect to $\xi_\perp$, as was shown in Sec. III D and is schematicized in Fig. 24(a). For this distortion, where $q$ is parallel to the cylinder axis we set $u(x,z)=u_0\sin(\vec{q}\cdot\vec{x})$. The associated splay elastic energy is then proportional to $K_1u_0^2q^4$. The sinusoidal dependence of the calculated energy is removed by averaging over many wavelengths. This low energy distortion involves only molecular splay of the polymer chains, an orientational rather than size perturbation. The perturbation for $u$ which includes only the distortions of compression and dilation (not splay) is $u(x,z)=u_0\sin(\vec{q}\cdot\vec{z})$, where the distortional wave number $q$ is now perpendicular to the microdomain axis [Fig. 24(b)]. The energy density for compression and expansion of the repeat spacing is proportional to $\overline{B}u_0^2q^2$. The ratio of these two distortional energies (splay to compressibility) is $(K_1/\overline{B})q^2$. The ratio of $K_1/\overline{B}$ is commonly denoted as $\lambda^2$, where $\lambda$ has units of distance and is comparable to a fraction of the repeat spacing of the microdomains. The ratio of distortional energies is then written as $(\lambda q)^2$. Amundson and co-workers showed that $\lambda$ can be calculated for copolymer systems [73]; analysis reveals that $\lambda\sim d/10$ here, consistent with that of most nematic systems. We set our wave number $q$ equal to $2\pi/\xi_2$, which we approximate as $2\pi/10d$ for the well-coarsened samples. This results in the ratio of distortions as $(\lambda q)^2\sim10^{-3}$, which shows that a splay distortion is three orders of magnitude lower than a compressibility distortion. In Sec. VI E we measure the upper bound on $\lambda$ to be $d/2$, resulting in an upper bound of the energetic ratio of 1/10. This large ratio in the distortional modes results in a pattern which displays molecular splay with very little microdomain spacing distortion.

### D. Disclination characterization—measurement of elastic constant anisotropy

Well-coarsened samples exhibit disclinations separated by dozens of repeat spacings which can be used to measure the anistropy in elastic constants [52,74]. Examples of both positive and negative disclinations are shown in Figs. 3(b) and 7(c,d). The form of the strain field about a disclination is determined by the energetic cost of the associated deformation. The strain energy density $f$ for a nematic system (ignoring the deformations of layer compression and dilation in smectics for now) is shown below where $\vec{n}$ is the local director orientation,

$$f=\frac{1}{2}K_1(\vec{\nabla}\cdot\vec{n})^2+\frac{1}{2}K_2(\vec{n}\cdot\vec{\nabla}\times\vec{n})^2+\frac{1}{2}K_3(\vec{n}\times\vec{\nabla}\times\vec{n})^2. \tag{6.4}$$

Each of the three lowest order deformations—molecular splay, twist, and bend—are represented by the elastic constants $K_1$, $K_2$, and $K_3$ and the associated expressions above, respectively [51]. Since our system is two dimensional, we do not have twist and the anistropy of $K_1$ and $K_3$ completely determines the strain field of the observed disclinations. We take advantage of this to measure a lower bound on the anistropy $\epsilon$ in elastic constants, where $\epsilon=(K_3-K_1)/(K_1+K_3)$, by quantitatively examining the director fields of disclinations. Again we wish to emphasize that the patterns examined here are not equilibrium structures, but these observations pertain to the entire coarsening process, with the exception of the poorly ordered patterns seen at short annealing times. Therefore, we believe that the analysis pertains to the equilibrium state as well.

The strain field about a disclination is characterized by the director field $\theta$ as a function of azimuthal angle $\phi$ [see Fig. 25(a)]. In the simplest single-constant approximation, $K_1=K_3$, forcing $\epsilon=0$ and the director field $\theta(\phi)$ about a disclination is a linear function in $\phi$. Similarly low values of elastic constant anisotropy are often seen in nematics. For $\epsilon\ll1$, a perturbation to the equiconstant case can be used, which facilitates the generation of the function associated with the director field [75,76]. This perturbation is not useful for the smectic case here, where $\epsilon\sim1$ and numerical calculations were necessary to generate the predicted form of $\theta(\phi)$ for a given $\epsilon$,

$$\phi=p\int_0^{\theta-\phi}[(1+\epsilon\cos2x)/(1+p^2\epsilon\cos2x)]^{1/2}\partial x, \tag{6.5}$$

where $p$ is defined as

$$\pi=(s-1)p\int_0^{\pi}[(1+\epsilon\cos2x)/(1+p^2\epsilon\cos2x)]^{1/2}\partial x. \tag{6.6}$$

In smectic systems, the fixed layer spacing (in our case largely determined by the polymer's radius of gyration) dictates that bend is more energetically costly than splay, forcing $K_3\gg K_1$. Discussion and illustration of these two distortions can be found in Sec. III D and Figs. 7(a) and 7(b). We can directly measure this ratio by examining the director fields about a disclination and comparing it to the predicted functional form [52,74]. Our measurements focus on positive rather than negative disclinations as the strain field of the former deviates greater from the equiconstant cases, facilitating greater accuracy in measuring $\epsilon$. We also observe that

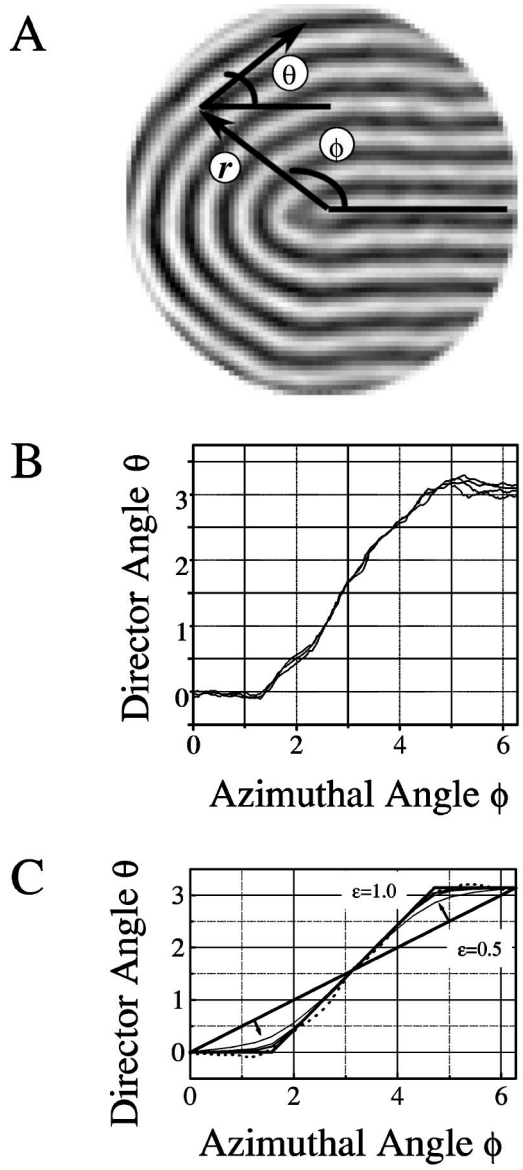


FIG. 25. (a) An SEM image of a $+\frac{1}{2}$ disclination for which the director strain field $\theta(r,\phi)$ is examined to measure the anisotropy in the elastic constants. The cylinders appear lighter. The director is measured by appropriate manipulation of the local gradient of the image intensity. (b) Measured values of $\theta(r,\phi)$ at several radii ($r=2.9,4.4,5.9,8.8d$) as a function of azimuthal angle $\phi$. The four traces of $\theta(\phi)$ largely overlap, confirming that the director field is relatively insensitive to the chosen radius, as long as neighboring disclinations are sufficiently far away. Note that the director field is constant for $\phi<\pi/2$ and $\phi$ for $\phi>3\pi/2$. Between these values, the director angles increase linearly with a slope of about unity. This is largely consistent with a high anisotropy $\epsilon$ with $K_1 \ll K_3$. (c) We present the average of $\theta(r=4.4d,\phi)$ for five disclinations (dashed line) and the calculated values of $\theta(r,\phi)$ for several values of $\epsilon$. The calculated $\theta(r)$ fields include $\epsilon=0$ (thick line of constant slope 1/2 with label), $\epsilon=1.0$ (thick line with zero slope for $\phi<\pi/2$, unity slope for $\pi/2<\phi<3\pi/2$, and zero slope for $\phi>3\pi/2$, with label). The three smooth thin lines are of increasing value of $\epsilon$ (0.7, 0.9, 0.95) as one proceeds along the direction of either arrow, roughly perpendicular to the line of $\epsilon=0.5$. Note that the measured $\theta(r)$ trace is closest to $\epsilon=0.95$.

negative disclinations consistently contain dislocations, which would either invalidate or complicate this analysis. [See Fig. 3(d) or 7(d).]

A $+\frac{1}{2}$ disclination from a well-coarsened sample is shown in Fig. 25(a). This disclination is chosen so as to be largely free of nonequilibrium structures, such as kinks, and sufficiently far away from other defects such that its own strain field dominates the director field. Our coordinate system origin for analysis is the disclination core. The director field was measured as described in the experimental section. We plot the director field as a function of angle at four radii ($r=2.9d,4.4d,5.9d,8.8d$) to show the insensitivity of the director field to the particular chosen radius [Fig. 25(b)]. Note the high nonlinearity of $\theta$ as a function of $\phi$. The director field $\theta$ fluctuates about zero for $\phi<\pi/2$, then increases with a slope of about 1.0, then levels off at $\pi$ for $\phi>3\pi/2$. This is consistent with $K_3 \gg K_1$, i.e., $\epsilon \sim 1$. To minimize the influence of the director field on the particular strain field of an individual defect (which may have kinks or the subtle influence from far away defects), we average the strain field at $r=4.4d$ over five disclination defects. This radius was chosen due to its proximity to the disclination cores, where the strain is the highest, yet a distance at which the higher dislocation density near the core only begins to increase. We compare this to the predicted functional forms of the director fields in Fig. 25(c). A fit to this data can be made to this plot using the functional form of Eqs. (6.5) and (6.6), yielding a lower bound for the anisotropy of $K_3/K_1 \sim 40$, or $\epsilon \sim 19/20$. We note that the limit on the upper bound is set by the accuracy of our director angle measurements and by our patience in performing the numerical calculations in extracting the angular dependence of $\theta$. This high ratio of $K_3/K_1$ originates from the high energetic cost of deviations from a fixed repeat spacing (and hence molecular bend) and is consistent with our interpretation of a single layer of cylindrical microdomains as a 2D smectic.

### E. Dislocation characterization—measurement of λ

The strain fields of dislocations allow us to measure the smectic penetration depth λ, a measure of the relative cost of the dominant distortions of splay and compressibility. The length scale λ is defined as the square root of the ratio of elastic constants $\sqrt{K_1/\bar{B}}$, where $K_1$ is molecular splay and $\bar{B}$ is the layer compressibility at constant density. Measurement of λ requires choosing an isolated dislocation (or a closely spaced cluster) which is far away from the strain fields of other disclinations or dislocations, measuring its orientational field, and comparing to that predicted by elastic strain theory. Using the standard nomenclature of the Burgers vector oriented along the $\hat{z}$ axis and the layers parallel to the $\hat{x}$ axis, the strain on the director angle $\theta$ [defined as Fig. 25(a)] is [51,58,77]

$$\theta = \frac{d}{4\pi^{1/2}} \frac{1}{(\lambda z)^{1/2}} \exp(-x^2/4\lambda z). \tag{6.7}$$

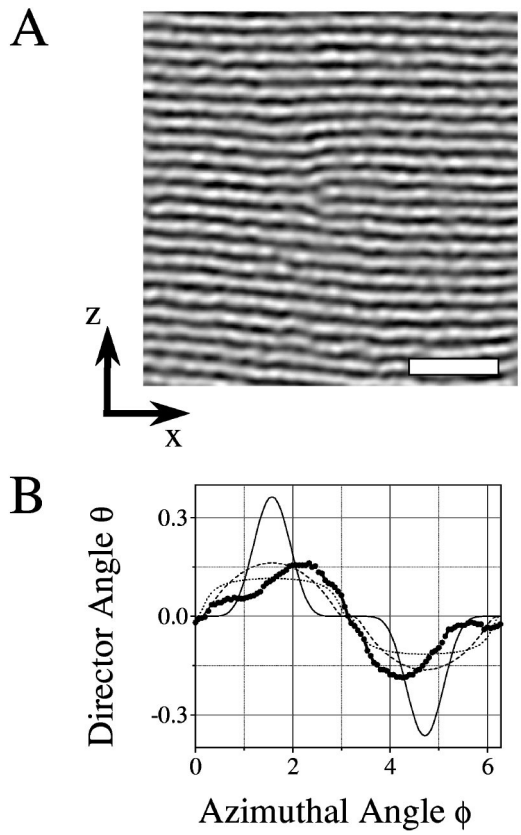


FIG. 26. (a) An AFM image of an isolated edge dislocation (center) in an otherwise strain-free region of a cylindrical microdomain forming sample. The protrusions along the individual cylinders (lighter) are artificacts of the AFM tip. The cylinders are light and the matrix is dark. Bar=100 nm. (b) Measured director strain field $\theta(r=1.5d,\phi)$ (line with circles) of microdomains as a function of azimuthal angle. As a comparison we show the theoretical director strain field for values of $\lambda=0.1d$ (solid line), $0.5d$ (dashed line), and $1.0d$ (dotted line), centered on the dislocation core. For $\lambda=0.1d$ to $1.0d$, the peaks sequentially lessen in magnitude and widen. Note that for $\lambda \ll d$, the director strain is concentrated into peaks of high magnitude at $\phi=\pi/2$ and $\phi=3\pi/2$. For $\lambda$ comparable to $d$, the strain diffuses throughout $\phi$ such that the peaks in $\theta$ become wider and of lower magnitude. From these theoretical strain fields we estimate an upper bound of $\lambda \sim d/2$ for this system. Instrumental and annealing constraints severely limit our ability to obtain a lower bound.

This equation can then be cast into a more useful form for our purposes where we describe $\theta$ as a function of azimuthal angle $\phi$ and radius $r$,

$$\theta = \frac{d}{4\pi^{1/2}} \frac{1}{(\lambda r \sin\phi)^{1/2}} \exp[-(r\cos^2\phi)/4\lambda \sin\phi]. \tag{6.8}$$

Figure 26(a) shows an isolated dislocation in the center of an AFM image obtained from a PS-PEP 5-13 film which was annealed at 423 K for $\approx$14 h. This film consists of two layers of cylinders (white). While consistent strain fields were observed in films with single layers of microdomains, films containing two layers of microdomains exhibited longer correlation lengths (at least on the upper layer) for this copolymer system. Dislocations were therefore farther apart on average and produced strain fields which were less perturbed by nearby defects. The accuracy of the measurement of the cylinder orientation is limited by the mottled nature of the cylinder, an artifact introduced by AFM. This artifact is absent in the higher resolution of electron microscopy, but the PS-rich copolymers (e.g., SI 30-11) examined by electron microscopy exhibited lower correlation lengths and hence higher densities of defects. Analysis revealed that the lower density of defects observed in the PS-PEP 5-13 system was the most important factor for accurate measurements of $\lambda$ and hence all analysis presented here originates from AFM data. This mottling limits us to measuring an upper bound on $\lambda$.

Dislocation cores were identified as the center of the terminated cylinder or a cylinder which bifurcated into two. The orientational field $\theta$ was measured as a function of azimuthal angle $\phi$ (similar to that about a disclination in Fig. 25) about the dislocation center for several radii and many dislocations. The radius of $1.5d$ was determined to be the optimal location—a compromise between the strong influence of the dislocation strain field for small radii while facilitating accurate measurements of the local microdomain orientation by not being too close to the dislocation core. The strain fields at distances significantly greater than this were too strongly influenced by other defects. The influence of other disclinations and dislocations on the measured strain field was minimized by averaging the strain field over that for four dislocations, but a large amount of asymmetry is still quite evident [Fig. 26(b)]. The best fit to the strain field yields an upper bound for $\lambda$ of $d/2$. As a comparison, the calculations of Amundson and Helfand suggest that $\lambda$ for the SI 30-11 copolymer studied here should be $0.1d$, consistent with an upper bound of $0.5d$ [73].

## VII. FINGERPRINTS

There is a striking similarity between the pattern of block copolymer microdomains shown in Fig. 3(b) and the dermatoglyphic prints on the palms of our hands and the soles of our feet. This similarity is dictated by the similar topological constraints, as both are intrinsically director rather than vector fields [78,79]. While we have investigated the academic problem of coarsening in a 2D smectic here, one could investigate the development of dermatoglyphs in animals as well. The community which investigates fingerprints observes the same topological defects as we do, but $+\frac{1}{2}$ disclinations are referred to as loops and $-\frac{1}{2}$ disclinations as triradii. There is general agreement that dermatoglyphs serve two functions: increasing one's gripping ability and acting as a stitching to secure the epidermis to the dermis layer. The development of dermatoglyphics in humans occurs around the third month of gestation and the resulting pattern is both environmentally and genetically determined—identical twins do not have identical fingerprints (albeit similar) [80–82]. One significant difference in the pattern development of dermatoglyphs (opposed to 2D smectics) is the fact that they originate at isolated regions (e.g., central point of the tips of

fingers) and proceed from the distal to proximal portions of the limb, rather than forming ubiquitously and straightening out, as our system does. Additionally, volar pads on palms and finger tips may play a role as their regression occurs at the same time as the development of ridges. Penrose has pointed out that the origin of dermatoglyphs [83] must not be from a vector field as their symmetry is that of a director. Rather, the process which brings about patterns on hands must be from a field with a tensor character, such as stress or strain, perhaps resulting from surface curvature. Supporting evidence is provided by the observation that fingerprints in the absence of whorls or defects produce lines which follow the path of greatest curvature. For example, it is observed that defect-free dermatoglyphics form rings about digits; the ridges run perpendicular to the long axis of the finger [81,84].

## VIII. SUMMARY

In closing, we have demonstrated that a 2D smectic system has additional topological constraints, which lower the kinetic exponents to 1/4 from the value of 1/2 observed in 2D nematic systems. Pattern coarsening occurs predominantly by an unexpected annihilation process involving three or four disclinations such that a minimum number of dislocations is produced. We quantitatively demonstrated that the orientational correlation length $\xi_2$ increases with a $t^{1/4}$ power law during coarsening as the disclination density $\rho_{\pm}$ decreases. Throughout the experiment, the density of $+\frac{1}{2}$ disclinations equals the density of $-\frac{1}{2}$ disclinations, suggesting that annihilation of opposite winding numbers was occurring. Moreover, the magnitude of the correlation length directly scaled with $\rho_{\pm}^{-1/2}$, suggesting that the dynamics of $\xi_2(t)$ can be understood by studying the interaction of topological defects. Dislocations were examined as well, and it was shown that the dislocation density is about ten times as large as the disclination density. The dislocation density decreased during coarsening, in part due to dislocation-dislocation annihilation events. The dislocation density was shown to be higher nearer the cores of disclinations, and the highest densities were seen near the cores of $-\frac{1}{2}$ disclinations, perhaps to alleviate the strain of its particular topology.

After examining this coarsening process statistically, a second copolymer system was examined via atomic force microscopy, which allowed for tracking of individual defects. Pairwise annihilation of disclinations was shown to be suppressed, and this was explained by pointing out that pairwise disclination annihilation processes necessarily produce dislocations, which we interpet as being uphill in energy. However, multidisclination annihilation events (such as quadrupoles) were observed to occur an order of magnitude more frequently. Such multidisclination events would result in lowered kinetic exponents and a model is proposed to explain this. Our model includes the necessity of dislocation exchange during annihilation disclination; this was further supported by examining annihilation events involving three disclinations.

To our knowledge, this is the first experimental exploration of the coarsening of a 2D smectic. Simulations, however, have examined this problem for over a decade, revealing a kinetic exponent similar to the one quarter that we have measured. A variety of systems have been examined, with both conserved and nonconserved dynamics, but similar low fractional exponents are typically measured. Whereas the origin of the exponent was unclear from simulations, we argue that it arises from the particular topology of striped systems, which disfavor pairwise disclination annihilation.

In addition to the work on coarsening, equilibrium properties were extrapolated by measurements on well-annealed samples. We show that translation order is destroyed by fluctuations in the local director field rather than by dislocations. This is consistent with Toner and Nelson's predictions for a 2D smectic. Measurements of the ratios of elastic constants $K_1/K_3$ and $K_1/\overline{B}$ were made by examining the strain fields from disclinations and dislocations, respectively. While these measurements provided only upper bounds, the values measured are consistent with systems of this symmetry.

Some open questions remain for future studies which could be answered through either simulation or experimentation.

(i) How general is this 1/4 exponent? Does it apply to both driven and nondriven systems?

(ii) How sensitive is this exponent to temperature? If raising the temperature and bringing the system closer to melting reduces barriers to defect coalescence, should this not change the exponent? Perhaps even allow it to be 1/2 expected for a nematic?

(iii) What are the details of dislocation motion? In our current configuration, the motion of dislocations is too fast to be satisfactorily captured, but a truly *in situ* analysis of microdomain motion could reveal this. Surprisingly, climb has been predicted to be more favorable than glide for smectic systems [72].

(iv) What is the effect of an alignment facet on the microdomain orientation? Presumably cylindrical microdomains orient parallel to a facet, but at what rate does the alignment propagate away from the facet? How far does it propagate?

(v) If diffusivity of polymer chains is higher when parallel to microdomains opposed to perpendicular (the latter requiring mixing of blocks), what is the effect of the ratio of diffusivities on the kinetic exponents? Does dislocation glide require diffusion perpendicular to the microdomains?

(vi) What is the spatial dependence of the interaction force of pairs of quadrupoles of disclinations—can these be simulated so that the pattern evolution can be examined with virtually infinite time resolution, in contrast to our coarse time scale experimentally?

With the application of AFM to thin copolymer films, these questions become straightforward to investigate. Temperature-controlled heater stages with heated tips have finally begun to allow investigators to examine these questions *in situ*, which promises to reveal new insights into pattern formation. Additionally, the phenomenal increase in computational power during the past decade allows investigators to examine larger systems where correlation functions can be calculated quickly and accurately. We suggest that pattern formation and evolution in copolymer realizations

will prove a rich field to further our understanding of topology and physics.

## ACKNOWLEDGMENTS

This work was supported by the National Science Foundation through the Princeton Center for Complex Materials (DMR-9400362 and DMR-9809483), through DMR-9802468, and the donors of the American Chemical Society Petroleum Research Fund (35207-AC5,7). We gratefully acknowledge the support of Michael Rooks, Dustin Carr, and Gabor Nagy at the Cornell Nanofabrication Facility, where electron microscopy was performed. Atomic force microscopy was made possible by the efforts of Nan Yao and Jane Woodruff at the Princeton Materials Institute. We are indebted to Yi Xiao for computational assistance. We gratefully acknowledge useful discussions with S. Milner, D. Nelson, N. Balsara, and T. Witten. This work was made possible by the assistance of S. Magonov during a visit to Digital Instruments by one of us (C.H.). D.A.V. gratefully acknowledges support from the National Research Council of Argentina (CONICET) and Universidad Nacional del Sur.

[1] C. Bowman and A. C. Newell, Rev. Mod. Phys. **70**, 289 (1998).
[2] D. R. Nelson and B. I. Halperin, Phys. Rev. B **19**, 2457 (1979).
[3] J. Toner and D. R. Nelson, Phys. Rev. B **23**, 316 (1981).
[4] B. I. Halperin and D. R. Nelson, Phys. Rev. Lett. **41**, 121 (1978).
[5] C. Murray, in *Bond-Orientational Order in Condensed Matter Systems*, edited by K. Strandberg (Springer-Verlag, New York, 1992).
[6] M. Seul and D. Andelman, Science **267**, 476 (1995).
[7] F. S. Bates and G. H. Fredrickson, Annu. Rev. Phys. Chem. **41**, 525 (1990).
[8] F. S. Bates, Science **251**, 898 (1991).
[9] M. J. Fasolka and A. M. Mayes, Annu. Rev. Mater. Sci. **31**, 323 (2001).
[10] K. Amundson, E. Helfand, X. Quan, S. D. Hudson, and S. D. Smith, Macromolecules **27**, 6559 (1994).
[11] A notable exception to this general observation would be the chemically heterogeneous surfaces formed by the polystyrene-poly(methyl methacyrlate) copolymer system. See, for example, J. M. Jaeger and T. L. Morkved, Europhys. Lett. **40**, 643 (1997).
[12] C. Harrison, M. Park, P. Chaikin, R. Register, D. Adamson, and N. Yao, Polymer **30**, 2733 (1998).
[13] While this diagram applies to polystyrene-polyisoprene copolymers, the analogous morphology of thin films of polystyrene-(poly-ethylene-propylene) copolymers is currently being investigated.
[14] H. J. Dai, N. P. Balsara, B. A. Garetz, and M. C. Newstein, Phys. Rev. Lett. **77**, 3677 (1996).
[15] M. C. Newstein, B. A. Garetz, N. P. Balsara, M. Y. Chang, and H. J. Dai, Macromolecules **31**, 64 (1998).
[16] K. Amundson and E. Helfand, Macromolecules **26**, 2698 (1993).
[17] M. Park, C. Harrison, P. M. Chaikin, R. A. Register, and D. H. Adamson, Science **276**, 1401 (1997).
[18] C. Harrison, M. Park, P. M. Chaikin, R. A. Register, and D. H. Adamson, J. Vac. Sci. Technol. B **16**, 544 (1998).
[19] R. D. Peters, X. M. Yang, Q. Wang, J. J. de Pablo, and P. F. Nealey, J. Vac. Sci. Technol. B **18**, 3530 (2000).
[20] C. Harrison, M. Park, R. A. Register, D. H. Adamson, P. Mansky, and P. M. Chaikin, US Patent No. 5,948,470 7 September (1999).
[21] W. A. Lopes and H. M. Jaeger, Nature (London) **414**, 735 (2001).
[22] M. Park, P. M. Chaikin, R. A. Register, and D. H. Adamson, Appl. Phys. Lett. **79**, 257 (2001).
[23] R. R. Li, P. D. Dapkus, M. E. Thompson, W. G. Jeong, C. K. Harrison, P. M. Chaikin, R. A. Register, and D. H. Adamson, Appl. Phys. Lett. **76**, 1689 (2000).
[24] T. L. Morkved, M. Lu, A. M. Urbas, E. E. Ehrichs, H. M. Jaeger, P. Mansky, and T. P. Russell, Science **273**, 931 (1996).
[25] P. Mansky, J. DeRouchey, T. P. Russell, J. Mays, M. Pitsikalis, T. Morkved, and H. M. Jaeger, Macromolecules **31**, 4399 (1998).
[26] T. Thurn-Albrecht, J. DeRouchey, T. P. Russell, and H. M. Jaeger, Macromolecules **33**, 3250 (2000).
[27] T. Thurn-Albrecht, J. Schotter, C. A. Kastle, N. Emley, T. Shibauchi, L. Krusin-Elbaum, K. Guarini, C. T. Black, and M. T. Tuominen, Science **290**, 2126 (2000).
[28] R. A. Segalman, H. Yokoyama, and E. J. Kramer, Adv. Mater. **12**, 1152 (2001).
[29] C. Park, C. De Rosa, and E. Thomas, Macromolecules **34**, 2602 (2001).
[30] L. Zhuang, S. Y. Chou, R. A. Register, C. K. Harrison, and P. M. Chaikin (unpublished).
[31] M. Morton and L. J. Fetters, Rubber Chem. Technol. **48**, 359 (1975).
[32] J. L. Adams, D. J. Quiram, W. W. Graessley, R. A. Register, and G. R. Marchand, Macromolecules **31**, 201 (1998).
[33] C. Lai, W. B. Russel, G. R. Marchand, and D. H. Adamson, Macromolecules **33**, 3461 (2000).
[34] L. J. Fetters, D. J. Lohse, D. Richter, T. A. Witten, and A. Zirkel, Macromolecules **27**, 4639 (1994).
[35] I. W. Hamley, *The Physics of Block Copolymers*, 1st ed. (Oxford University Press, New York, 1998).
[36] C. Harrison, P. M. Chaikin, D. A. Huse, R. A. Register, D. H. Adamson, A. Daniel, E. Huang, P. Mansky, T. P. Russell, C. J. Hawker, E. A. Egolf, I. V. Melnikov, and E. Bodnenschatz, Macromolecules **33**, 857 (2000).
[37] G. Coulon, D. Ausserre, and T. P. Russell, J. Phys. (France) **51**, 777 (1990).
[38] While an ion gauge was used to measure the base pressure of the vacuum oven, its operation had a detrimental effect on thin polymer films, perhaps due to ions produced by its discharge. Polymer films near the ion gauge lost their susceptibility to $OsO_4$ staining, and ceased to coarsen. Hence after determining the robustness of the vacuum apparatus all polymer film annealing was subsequently performed with the ion gauge off.

[39] S. Sze, *VLSI Technology*, 2nd ed. (McGraw-Hill, New York, 1988), p. 184.
[40] C. K. Harrison, M. Park, P. M. Chaikin, R. A. Register, and D. H. Adamson, Macromolecules **31**, 2185 (1998).
[41] A prototype thermal accessory from Digital Instruments. This has subsequently been replaced with the Thermal Accessory for Multimode and High Temperature Accessory for Multimode.
[42] J. Hahm, W. A. Lopes, H. M. Jaeger, and S. J. Sibener, J. Chem. Phys. **109**, 10111 (1998).
[43] S. N. Magonov, J. Cleveland, V. Elings, D. Denley, and M. H. Whangbo, Surf. Sci. **389**, 201 (1997).
[44] Most details of our computational techniques can be found in C. Harrison, thesis Princeton University, 1999.
[45] J. C. Russ, *The Image Processing Handbook*, 2nd ed. (CRC Press, Ann Arbor, 1995).
[46] P. G. de Gennes and J. Prost, *The Physics of Liquid Crystals*, 2nd ed. (Oxford Science, New York, 1993).
[47] J. Forrest and K. Dalnoki-Veress, Adv. Colloid Interface Sci. **94**, 167 (2001).
[48] J. Ferry, *Viscoelastic Properties of Polymers*, 3rd ed. (Wiley, New York, 1980).
[49] Lodge and co-workers have performed extensive measurements of diffusion in copolymer systems. See M. C. Dalvi, C. E. Eastman, and T. P. Lodge, Phys. Rev. Lett. **71**, 2591 (1993).
[50] S. Chandrasekhar, *Liquid Crystals*, 2nd ed. (Cambridge University Press, New York, 1992), pp. 338–339.
[51] M. Kleman, *Points, Lines and Walls* (Wiley, New York, 1983).
[52] The elastic constants more strongly affect $+\frac{1}{2}$ disclinations because negative disclinations have more nodes (regions where the energetic cost does not deviate from the equiconstant case) than positive disclinations. See S. D. Hudson and E. L. Thomas, Phys. Rev. Lett. **62**, 1993 (1989).
[53] The Burgers vector construction is performed on a closed loop path integral and measures the net number of dislocations inside by counting the net number of layer spacings traversed. For a full description, see books by Kleman [51], Prost [46], or Chandrasekhar [50].
[54] B. Yurke, A. N. Pargellis, T. Kovacs, and D. A. Huse, Phys. Rev. E **47**, 1525 (1993).
[55] C. Liu and M. Muthukumar, J. Chem. Phys. **106**, 7822 (1997).
[56] C. W. Meyer, G. Ahlers, and D. S. Cannell, Phys. Rev. A **44**, 2514 (1991).
[57] Y. Hu, R. Ecke, and G. Ahlers, Phys. Rev. E **48**, 4399 (1993).
[58] E. Guazzelli, E. Guyon, and J. E. Wesfreid, Philos. Mag. A **48**, 709 (1983).
[59] E. Guvois-Violette, E. Guazzelli, and J. Prost, Philos. Mag. A **48**, 727 (1983).
[60] M. Seul and R. Wolfe, Phys. Rev. Lett. **68**, 2460 (1992).
[61] M. Seul and R. Wolfe, Phys. Rev. A **46**, 7534 (1992).
[62] L. Purvis and M. Dennin, Phys. Rev. Lett. **86**, 5898 (2001).
[63] Q. Hou and N. Goldenfeld, Physica A **239**, 219 (1997).
[64] M. C. Cross and D. I. Meiron, Phys. Rev. Lett. **75**, 2152 (1995).
[65] T. Taneike and Y. Shiwa, J. Phys.: Condens. Matter **9**, L147 (1997).
[66] K. R. Elder, J. Vinals, and M. Grant, Phys. Rev. Lett. **68**, 3024 (1992).
[67] Y. Shiwa, T. Taneike, and Y. Yokojima, Phys. Rev. Lett. **77**, 4378 (1996).
[68] A. J. Bray, Phys. Rev. E **58**, 1508 (1998).
[69] J. J. Christensen and A. J. Bray, Phys. Rev. E **58**, 5364 (1998).
[70] F. L. Somer Jr., G. S. Canright, T. Kaplan, K. Chen, and M. Mostoller, Phys. Rev. Lett. **79**, 3431 (1997).
[71] F. L. Somer Jr., G. S. Canright, and T. S. Kaplan, Phys. Rev. E **58**, 5748 (1998).
[72] M. Kleman and C. E. Williams, J. Phys. (France) Lett. **35**, L-49 (1974).
[73] K. Amundson and E. Helfand, Macromolecules **26**, 1324 (1993).
[74] I. E. Dzyaloshinkskii, Zh. Eksp. Teor. Fiz. **58**, 1443 (1970) [Sov. Phys. JETP **31**, 773 (1970)].
[75] J. Nehring and A. Saupe, J. Chem. Soc., Faraday Trans. 2 **68**, 1 (1972).
[76] S. D. Hudson, J. W. Fleming, E. Gholz, and E. L. Thomas, Macromolecules **26**, 1270 (1993).
[77] P. G. de Gennes, C. R. Acad. Sci. Paris, Ser. B **275**, 939 (1972).
[78] L. S. Penrose, Nature (London) **205**, 544 (1965).
[79] L. S. Penrose, Sci. Am. **221(6)**, 73 (1969).
[80] H. Cummins and C. Midlo, *Finger Prints, Palms and Soles: An Introduction to Dermatoglyphics* (The Blakiston Company, Philadelphia, 1943).
[81] D. Z. Loesch, *Quantitative Dermatoglyphics: Classification, Genetics, and Pathology* (Oxford University Press, Oxford, 1983).
[82] J. D. Murray, *Mathematical Biology*, 2nd ed. (Springer, New York, 1993).
[83] R. Penrose, Ann. Hum. Genet. **42**, 435 (1979).
[84] L. S. Penrose and P. T. Ohara, J. Med. Genet. **10**, 201 (1973).